

## HOT JUPITER MAGNETOSPHERES

GEORGE B. TRAMMELL, PHIL ARRAS, ZHI-YUN LI  
*Draft version November 2, 2010*

### ABSTRACT

The upper atmospheres of close-in gas giant exoplanets (“hot Jupiters”) are subjected to intense heating and tidal forces from their parent stars. The atomic (H) and ionized (H<sup>+</sup>) hydrogen layers are sufficiently rarefied that magnetic pressure may dominate gas pressure for expected planetary magnetic field strength. We examine the structure of the magnetosphere using a three-dimensional (3D) isothermal magnetohydrodynamic model that includes: a static “dead zone” near the magnetic equator containing gas confined by the magnetic field; a “wind zone” outside the magnetic equator in which thermal pressure gradients and the magneto-centrifugal-tidal effect give rise to a transonic outflow; and a region near the poles where sufficiently strong tidal forces may suppress transonic outflow. Using dipole field geometry, we estimate the size of the dead zone to be several to tens of planetary radii for a range of parameters. Tides decrease the size of the dead zone, while allowing the gas density to increase outward where the effective gravity is outward. In the wind zone, the rapid decrease of density beyond the sonic point leads to smaller densities relative to the neighboring dead zone, which is in hydrostatic equilibrium. To understand the appropriate base conditions for the 3D isothermal model, we compute a simple one-dimensional (1D) thermal model in which photoelectric heating from the stellar Lyman continuum is balanced by collisionally-excited Lyman  $\alpha$  cooling. This 1D model exhibits a H layer with temperature  $T \simeq 5,000 - 10,000\text{K}$  down to a pressure  $P \sim 10 - 100$  nbar. Using the 3D isothermal model, we compute maps of the H column density as well as the Lyman  $\alpha$  transmission spectra for parameters appropriate to HD 209458b. Line-integrated transit depths  $\simeq 5 - 10\%$  can be achieved for the above base conditions, in agreement with the results of Koskinen et al. A deep, warm H layer results in a higher mass-loss rate relative to that for a more shallow layer, roughly in proportion to the base pressure. Strong magnetic fields have the effect of increasing the transit signal while decreasing the mass loss, due to higher covering fraction and density of the dead zone. Absorption due to bulk fluid velocity is negligible at linewidths  $\gtrsim 100 \text{ km s}^{-1}$  from line center. In our model, most of the transit signal arises from magnetically confined gas, some of which may be outside the L1 equipotential. Hence the presence of gas outside the L1 equipotential does not directly imply mass loss. We verify *a posteriori* that particle mean free paths and ion-neutral drift are small in the region of interest in the atmosphere, and that flux freezing is a good approximation. We suggest that resonant scattering of Lyman  $\alpha$  by the magnetosphere may be observable due to the Doppler shift from the planet’s orbital motion, and may provide a complementary probe of the magnetosphere. Lastly, we discuss the domain of applicability for the magnetic wind model described in this paper as well as the Roche-lobe overflow model.

### 1. INTRODUCTION

Hot Jupiters, the gas giant exoplanets found at small orbital radii,  $D \lesssim 0.1 \text{ AU}$ , present an opportunity to study planets orbiting in an extreme environment very close to their parent stars. They experience insolation levels  $\sim 10^4$  times greater than solar system gas giants. As a consequence of the high temperatures generated by EUV heating, the gas pressure scale height is comparable to the planetary radius, creating an extended upper atmosphere of gas potentially observable through transmission or reflection spectroscopy. Heating may also create an outward pressure force, complemented by outward centrifugal and tidal forces, which may drive an outflow leading to mass and angular momentum loss from the planet.

While most observational effort for the transiting planets has centered on the lower atmosphere, near the photospheres for optical and infrared continuum radiation at mbar-bar pressures, there has also

been progress in probing higher levels in the atmosphere. As these observations probe a larger area surrounding the planet, the transit depth is correspondingly larger than that from the photospheric radius,  $R_{\text{ph}}$ . Bound-bound atomic lines in the transmission spectrum from NaI (Charbonneau et al. 2002), HI (Vidal-Madjar et al. 2003, 2004; Ehrenreich et al. 2008), OI and CII (Vidal-Madjar et al. 2004), and SiIII (Linsky et al. 2010) have been observed for HD 209458b; HI in HD 189733b (Lecavelier Des Etangs et al. 2010); and MgII (Fossati et al. 2010), and possibly other species at lower signal to noise, in WASP-12b. Bound-free transitions from a population of hydrogen in the  $n = 2$  state have been detected in the transmission spectrum of HD 209458b (Ballester et al. 2007), although no bound-bound transitions from  $n = 2$  were found (Winn et al. 2004).

The large transit depths observed for the Lyman  $\alpha$  line in HD 209458b imply neutral H atoms occupy an occulting area equivalent to an optically thick disk extending out to several planetary radii, comparable to the Roche-lobe radius for this close-in planet. This

Department of Astronomy, University of Virginia, P.O. Box 400325, Charlottesville, VA 22904-4325

led Vidal-Madjar et al. (2003) to suggest that the H atoms are escaping from the planet, as they would no longer be bound to the planet outside the Roche-lobe radius. The presence of heavy atoms (C, O, etc.), whose scale height should be far smaller than that of the H atoms, was suggested to be due to a combination of efficient turbulent mixing and drag forces from the escaping gas, entraining the heavier elements in an outflow (Vidal-Madjar et al. 2004; García Muñoz 2007). Ben-Jaffel (2007) used archival HST data to rederive the transit depth, and challenged the claim that atmospheric escape was occurring, due to a derived transit depth that would imply the H atoms are within the Roche lobe radius. Two subsequent studies (Ben-Jaffel 2008; Vidal-Madjar et al. 2008) elucidated the dependence of transit depth on the analysis method and wavelength range studied. The recent study by Linsky et al. (2010) attempts to constrain the wind velocity in HD 209458b using the line profiles for the CII and SiIII lines.

Most theoretical efforts to explain the aforementioned observations invoke EUV heating to temperatures  $\sim 10^4$  K, creating a thermally driven, possibly transonic hydrodynamic outflow from the planet (Yelle 2004, 2006; Tian et al. 2005; García Muñoz 2007; Murray-Clay et al. 2009; Stone & Proga 2009). While initiated by outward gas pressure gradients, a thermally-driven wind can be significantly accelerated by the tidal gravity<sup>2</sup>. An alternative model is to treat atmospheric escape as Roche-lobe overflow (Gu et al. 2003; Li et al. 2010; Lai et al. 2010), assuming that the fluid can only reach the sound speed in the vicinity of the L1 Lagrange point.

For gas giants, H is the most abundant element and heating is dominated by photoionization of atomic H in the thermosphere (Yelle 2004). Photoionization leads to significantly ionized gas at high altitudes that is subject to magnetic forces. In light of the high ionization fraction, the planetary magnetic field, due to dynamo action in the planet’s core, may be dynamically important and affect density and velocity profiles in the upper atmosphere. This paper is a first attempt to include the effects of the planet’s magnetic field combined with tidal and centrifugal forces on upper atmosphere structure for hot Jupiters.

We model the magnetized, hot, rotating portion of the planet’s upper atmosphere in the context of magneto-hydrodynamic (MHD) outflows, the theory of which was originally developed for stars and accretion disks. Figure 1 shows a cartoon of the expected structure for the wind from an isolated object with a surface dipole field: the polar region supports an outflow while the equatorial region contains static, magnetically confined gas (see also Yelle 2004). This configuration applies interior to the magnetosphere-stellar wind interaction, for planets not too near the parent star. Near the parent star, tidal forces are an important consideration, and we will show that tides may strongly affect the density profile and size of the static region, and may even shut the wind off in the polar region.

In the first half of the paper (§ 2 through § 7), we develop a general theory of isothermal hot Jupiter magne-

<sup>2</sup> In this paper we will use the phrase “tidal gravity” to include the effect of both the stellar tide and the centrifugal force, assuming synchronized rotation (see § 5.)

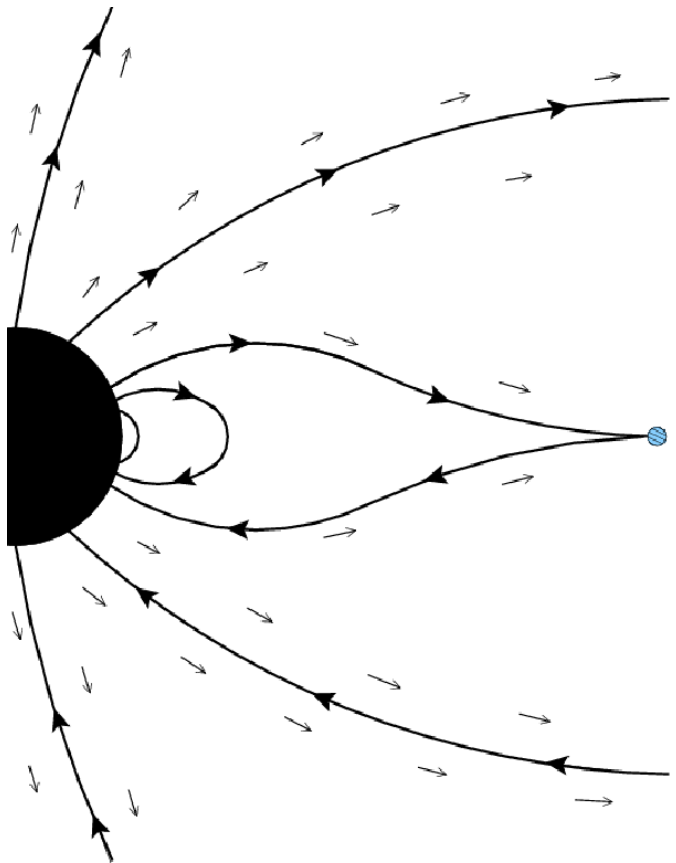


FIG. 1.— Schematic model for magnetic field structure (thick lines and arrows) and fluid velocity (thin arrows). In the polar “wind zone”, magnetic field lines are open allowing outflow. In the equatorial “dead zone” close to the planet, the gas has zero velocity and no outflow occurs. The dead zone ends in a cusp-type neutral point, denoted by the dashed circle at several planetary radii, outside of which field lines are open at all angles. This figure is characteristic of the weak tide limit, while in the strong tide limit the polar wind would be partially suppressed (see § 7).

tospheres. Section 2 discusses the problem setup and approximations used to obtain a solution. Planetary magnetic field strengths predicted by dynamo models are discussed in section 3. Section 4 discusses qualitative features of atmospheric structure, and motivation for the existence of a dead zone. Section 5 reviews the centrifugal and tidal forces, and discusses the projection of these forces along magnetic field lines. The structure of the dead zone is discussed in section 6, followed by the wind zone in section 7.

The second half of the paper (§ 8 through § 12) uses the Lyman  $\alpha$  transmission spectra to constrain parameters of the global 3D models. In section 8, we construct a 1D model in hydrostatic, thermal, and ionization balance to compute appropriate values for the base pressure and temperature for the 3D global models that we present in section 9. Mass loss rates are computed and spin-down torques are estimated, in section 10. Neutral H column density maps for the global models are used to illustrate the dependence on key parameters in section 11. Lyman  $\alpha$  transmission spectra in comparison with observations and scattering of stellar Lyman  $\alpha$  by the planet are presented in section 12. Finally, we compare and contrast our magnetic wind model with the standard Roche-lobe overflow model in section 13. Summary and discussion

are given in section 14. The MHD wind equations and ion-neutral coupling are discussed in Appendices A and B, respectively.

## 2. PROBLEM SETUP AND APPROXIMATIONS

In this section we outline the problem to be solved, and the simplifying assumptions used to find solutions. Except for section 8, this paper discusses a 3D isothermal model of the upper atmosphere. The isothermal model is parametrized by an effective sound speed, as well as the pressure at a fiducial radius. Appropriate values for these parameters are discussed in a simple 1D spherical model in section 8, including photoionization and thermal equilibrium.

In the 3D model, we compute approximate solutions of the one-fluid MHD equations with an inner boundary at the base of the warm H layer, and an outer boundary which extends to at least ten planetary radii (or one stellar radius). We treat the gas as having constant isothermal sound speed  $a = \sqrt{k_b T / \mu m_p}$ , where  $T$  is gas temperature of the fluid,  $\mu$  is the mean molecular weight,  $k_b$  is Boltzmann's constant, and  $m_p$  is the proton mass. At the inner boundary, the density and pressure are assumed to follow equipotentials. We assume the planet's rotation rate is synchronized with its orbital motion around the parent star, giving orbital and spin angular velocity  $\Omega$ . We work in a coordinate system centered on the planet and rotating at rate  $\Omega$ . The stellar gravity is included in the tidal approximation, and an effective potential  $U$  is composed of the planetary gravity, stellar gravity, and the centrifugal force. We specify a specific magnetic field geometry which is dipole near the planet and matches onto a radial field at the dead zone radius. We compute the ionization fraction with a simple, optically thin model applied to the derived gas densities of the MHD model. To summarize, we have made several simplifying assumptions in order to focus on the new physics arising from MHD effects. We now discuss these simplifying approximations in more detail.

The simultaneous inclusion of photoionization heating, chemical reactions and collisional coupling between different species, stellar tidal forces, and the simultaneous interaction with the stellar wind in the presence of magnetic field is a formidable problem. Our approach is to first ignore the interaction with the stellar wind, but to include the effect of the stellar tidal forces felt by the planet's atmosphere. The interaction with the stellar wind may alter the results of this paper in several ways (see e.g., Murray-Clay et al. 2009; Stone & Proga 2009). The stellar wind will limit the size of the magnetosphere, as determined by stress balance at the magnetopause (e.g., Preusse et al. 2007). Reconnection between field lines in the stellar wind and magnetosphere may lead to magnetospheric convection, limiting the high density region to be inside a plasmopause (Parks 2004), as for Earth. Finally, reconnection may also generate non-thermal plasma populations. We do not consider the interaction with the stellar wind in order to construct the simplest possible model.

Another key approximation is that we treat photoionization heating as being spherically symmetric, creating a hot layer uniformly over the planet. In reality, the night side temperature and ionization state may depend on day-night heat redistribution, and downward heat

conduction along field lines not in the planet's shadow. In perfect MHD, such redistribution would be highly constrained in the magnetically dominated upper atmosphere, but finite conductivity may allow field lines to slip through the gas (Gold 1959). Even on the day side, large gas density outside the Roche lobe may project a non-spherically symmetric shadow on the deeper layers.

Near the planet, the dynamo-generated, roughly dipole field from the planets core is expected to dominate. Moving outward, currents generated in the magnetosphere comb the field lines into a nearly radial direction beyond the dead zone radius. Such a geometry has been used before in the context of the stellar wind (Mestel 1968; Mestel & Spruit 1987; Okamoto 1974) and we will adopt it here. This field geometry will be implemented in the global models presented in section 9, and is motivated in the discussion of Appendix A.

Finally, the one-fluid approximation assumes that mean free paths are sufficiently small that relative motion of different species can be ignored. In Appendix B we will check this assumption *a posteriori* for our models, which estimate particle densities and velocities in the dead and wind zones. Specifically, we will show that the electron-proton-hydrogen atom gas is well coupled collisionally for the parameters of interest, and therefore the drift velocity is small and hydrogen atoms have short mean free paths in the dead zone region. As a consequence, neutral hydrogen atoms do not fly ballistically through the magnetosphere, and photoionization equilibrium is a good approximation when computing the ionization fraction. Further, we compute the rate at which magnetic field can drift relative to the fluid. For this thermal population of particles in the magnetosphere, we find that the dead zone gives the largest observable transit signal, and that the bulk of the hydrogen atoms in the dead zone are not escaping.

In the next section we will review expected magnetic field strengths for hot Jupiters.

## 3. EXPECTED MAGNETIC FIELD STRENGTHS

The importance of the magnetic field for the upper atmosphere depends critically on the field strength. However, the magnetic fields of hot Jupiters are currently unconstrained by observation. This section will use theoretical considerations to estimate likely field strengths for hot Jupiters.

Sánchez-Lavega (2004) computed that Rayleigh numbers in hot Jupiters are typically much larger than the critical Rayleigh number for thermal convection in the metallic core. Using estimates of the fluid velocity carrying the heat flux, he found that the magnetic Reynolds number is much larger than unity, and that dynamo action can occur. He argued that if the dynamo operated with Elsasser number of order unity, then  $B \sim (2\rho\Omega\lambda_B)^{1/2}$ , where  $\rho$  is the mass density and  $\lambda_B$  is the magnetic diffusivity. The dominant scaling important for hot Jupiters is then with rotation:  $B \propto \Omega^{1/2}$ . For synchronized planets with orbital periods of a few days, this scaling predicts that the field for hot Jupiters should be smaller than that of Jupiter (equatorial field  $B_{J,eq} = 4.3$  G) by a factor of a few.

The opposite conclusion may be drawn from the recent results of Christensen et al. (2009). As the rotation rate is increased above a critical value, the field strength no

longer increases with rotation rate, and dynamo simulations give a magnetic field strength  $B \sim (\rho F_{\text{core}}^2)^{1/3}$ , nearly independent of rotation rate and magnetic diffusivity, where  $F_{\text{core}}$  is the heat flux escaping from the conducting core. Christensen et al. (2009) show that this scaling applies to both planets and rapidly rotating, low mass stars over many orders of magnitude in heat flux. They argue that the dependence on  $F_{\text{core}}$  arises since it is the heat flux reservoir that sustains the magnetic field against Ohmic dissipation. To be in the saturated regime, the Rossby number  $Ro$  must satisfy  $Ro = V_{\text{ed}}/\Omega\ell \lesssim 0.1$ , where  $V_{\text{ed}}$  is the typical velocity of the eddies transporting heat, and  $\ell$  is the size of the conducting region;  $\ell \sim R$  for  $M_p \gtrsim 0.5M_J$ . Sánchez-Lavega (2004) estimated synchronized planets in few day orbits to have  $Ro \ll 0.1$ , using heat fluxes comparable to that of Jupiter. Hence these planets are expected to be in the saturated regime.

The large radii of hot Jupiters are currently not well understood, since the cooling and contraction time for passively cooling planets, even allowing for irradiation by the star, is far shorter than the age for a number of observed planets (e.g., Fortney & Nettelmann 2009). This has led to the suggestion that these planets are not passively cooling, but rather have an anomalous source of internal heating, which is as yet unidentified but balances the core cooling rate. To assess the required heating rates, Arras & Socrates (2009) computed cooling flux from the core for planets as a function of radius (their Figure 11; see Arras & Bildsten 2006, for a discussion of the cooling luminosity of irradiated hot Jupiters). For Jupiter-mass planets in the radius range  $R_{\text{ph}} = 1.3 - 1.5R_J$ , the cooling flux is larger than that of Jupiter by a factor  $10^2 - 10^3$ , for which the Christensen et al. (2009) scaling would give magnetic fields 5–10 times larger than Jupiter. Larger mass planets with the same radius would have larger cooling fluxes, and vice versa. For instance, WASP 12b, WASP 17b and TRES 4 have radii  $R_{\text{ph}} \sim 1.8R_J$  and masses in the range  $0.5 - 1.5M_J^3$ , for which the cooling fluxes would be  $10^3 - 10^4$  times higher than Jupiter, implying fields larger than Jupiter by factors of 10–20.

In summary, the recent results on dynamo theory from Christensen et al. (2009), and the assumption that hot Jupiter cores are subject to an externally powered heating (Arras & Socrates 2009), argue that field strengths may be up to an order of magnitude larger than that of Jupiter. We will take this as motivation to explore a wide range of parameter space for the magnetic field in our calculations.

In the next section, we show that the photoionized H and  $\text{H}^+$  layers are magnetically dominated for field strengths comparable to Jupiter or Saturn, and motivate the existence of a dead zone by a toy problem.

#### 4. DEAD ZONE-WIND ZONE STRUCTURE OF THE UPPER ATMOSPHERE

Yelle (2004) and García Muñoz (2007) presented detailed calculations of the transition between the molecular lower atmosphere ( $\text{H}_2$ ), the layer dominated by atomic hydrogen (H), and the ionized upper atmosphere ( $\text{H}^+$ ). In this paper, we restrict attention to the H and

$\text{H}^+$  regions, where the transmission spectrum is formed. The strong heating in these layers due to UV photon energy deposition raises the temperature to  $T \simeq 10^4$  K. As a consequence of the increased temperature and low mean molecular weight, the radial extent of the H and  $\text{H}^+$  layers ( $\gtrsim R_J$ ) is expected to be much larger than that of the  $\text{H}_2$  layer above the photosphere ( $\lesssim (0.1 - 0.2) \times R_J$ ).

We define the lower boundary of our wind model to be at the base of the warm ( $T \gtrsim 5000$  K) H layer, at base radius  $R$  and base pressure  $P_{\text{base}}$ . The base of the warm layer is a crucial parameter for the transit depth. As discussed in the phenomenological model of Koskinen et al. (2010), the transit depth of HD 209458b could be understood as being due to thermal  $\simeq 10^4$  K H gas extending down to  $\sim 10 - 100$  nbar pressures. In section 8, we compute a simple 1D model for ionization and thermal equilibria in the H and  $\text{H}^+$  layers which shows that such base conditions are indeed possible.

The Lyman  $\alpha$  transmission spectrum of HD 209458b shows absorption by the planetary atmosphere at linewidths  $\Delta v \gtrsim 100$  km  $\text{s}^{-1}$  from line center. At this linewidth, the cross section is  $\sigma_\nu \simeq 2 \times 10^{-19}$   $\text{cm}^2$  (see Figure 15). Optical depth unity requires a hydrogen column  $N_H \simeq 1/\sigma_\nu \simeq 5 \times 10^{18}$   $\text{cm}^{-2}$ . Assuming the gas is dominated by atomic hydrogen, the pressure at this level in the atmosphere is  $P \simeq gm_p N_H \simeq 2$  nbar ( $g/300$   $\text{cm s}^{-2}$ ) (see Figure 10). This is a factor  $\sim 10^8$  more rarefied than the optical photosphere for continuum radiation at pressure  $P_{\text{ph}} \simeq 100$  mbar. Magnetic forces dominate in this layer if  $B^2/8\pi \gtrsim 2$  nbar ( $g/300$   $\text{cm s}^{-2}$ ), implying a critical field strength  $B_{\text{crit}} \gtrsim 0.25$  G ( $g/300$   $\text{cm}^2 \text{s}^{-1}$ ) $^{1/2}$ . This is less than Jupiter’s equatorial magnetic field  $B_{J,\text{eq}} = 4.3$  G and comparable to Saturn’s equatorial field  $B_{S,\text{eq}} = 0.22$  G. Moving upward, if the gas pressure drops much faster than magnetic pressure, the atmosphere can become highly magnetically dominated — a magnetosphere.

The theory of thermally and magneto-centrifugally driven MHD winds gives guidance on the upper atmosphere structure in the magnetically dominated case (for a good review see Spruit 1996). Consider a thought experiment in which a non-magnetic spherically symmetric wind with velocity  $v_\infty$  and mass loss rate  $\dot{M}$  exists at time  $t < 0$ , and at time  $t = 0$  a dipole magnetic field is turned on. On which field lines can the wind overpower the magnetic forces and open the field lines to infinity? The magnetic pressure on the equator ( $\theta = \pi/2$ ) is weaker than at the footpoint (at angle  $\theta_b$ ) by a factor  $[B(\pi/2)/B(\theta_b)]^2 = [R/r(\pi/2)]^6 = \sin^{12} \theta_b$  (see eq.12). This powerful dependence on footpoint position means there are always field lines near the magnetic poles which open to infinity on which a wind can outflow (see Figure 1 for a cartoon). The reason is that at the equator, the wind ram pressure can overcome the steeply falling magnetic pressure at sufficiently large distance from the planet. If we assume the wind ram pressure decreases outward as  $\rho v^2 = \dot{M} v_\infty / 4\pi r^2$ , then the critical footpoint angle inside of which a “polar wind” occurs is  $\sin \theta_b \simeq \left( \dot{M} v_\infty / R^2 B_0^2 \right)^{1/8}$ . For fiducial polar magnetic field  $B_0 = 8.6$  G,  $R = 1.4R_J$ , (constant) flow speed  $v_\infty = 10$  km  $\text{s}^{-1}$  and mass loss rate  $\dot{M} = 10^{11}$  g  $\text{s}^{-1}$  (mo-

<sup>3</sup> <http://exoplanet.eu/catalog-transit.php>

tivated by the studies of Yelle 2004; García Muñoz 2007; Murray-Clay et al. 2009), we find the polar cap size occupied by open field lines is  $\theta_b \simeq 14^\circ$ , and the last closed field lines is at equatorial radius  $r(\pi/2) \simeq 16R$ . This static, closed field line region is referred to as the “dead zone” (Mestel 1968). These estimates suggest that the region within a few planetary radii, where the transit signal arises, is filled primarily with static gas in the dead zone, rather than outflowing gas, as has been previously assumed.

For close-in, tidally-locked planets, tides and centrifugal forces play a key role in upper atmosphere structure. In the next section we review the effective potential near the planet, and the projection of forces along dipole field lines.

### 5. TIDAL FORCE AND MAGNETIC GEOMETRY

Gas in the upper atmosphere of the planet is subject to three potential forces: gravity from the planet, tidal gravity from the star, and the centrifugal force due to the planetary rotation. For a synchronized planet, the centrifugal and tidal forces, or just tidal force for short, are comparable in strength, although their angular dependence is different. For position vector  $\mathbf{x} = (r, \theta, \phi)$  relative to the center of the planet, and star at position  $\mathbf{x}_* = (D, \pi/2, 0) = D\mathbf{e}_x$ , the sum of the three accelerations is

$$\mathbf{a}(\mathbf{x}) = -\nabla U(\mathbf{x}), \quad (1)$$

where the effective potential is given by

$$\begin{aligned} U(\mathbf{x}) &= -\frac{GM_p}{|\mathbf{x}|} - \frac{GM_*}{|\mathbf{x} - \mathbf{x}_*|} + \frac{GM_* \mathbf{x} \cdot \mathbf{x}_*}{|\mathbf{x}_*|^3} - \frac{1}{2} |\boldsymbol{\Omega} \times \mathbf{x}|^2 \\ &\simeq -\frac{GM_p}{r} - \frac{1}{2} \Omega^2 r^2 (f \sin^2 \theta - 1). \end{aligned} \quad (2)$$

Equipotentials are shown in Figure 6.2 of Kopal (1978). The longitude-dependent function  $f = 1 + 3 \cos^2 \phi$ . The vector angular velocity of the orbit is  $\boldsymbol{\Omega} = \Omega \mathbf{e}_z$ , where  $\mathbf{e}_z$  is normal to the orbital plane, and  $\Omega = [G(M_* + M_p)/D^3]^{1/2}$ . The first and second terms in eq.2 are the potential of the planet and star, respectively. The third term in eq.2 is due to the motion of the origin of the coordinate system. The last term in eq.2 is due to the centrifugal force. It may be shown that eq.2 is equivalent to the usual Roche potential with origin at the center of mass by combining the third and fourth terms. The form in eq.3 is an expansion in the limit  $r \ll D$ , and agrees with that for “Hill’s limit” found in Murray & Dermott (2000) when evaluated in the orbital plane ( $\theta = \pi/2$ ).

The accelerations are given by

$$a_r = -\frac{\partial U}{\partial r} = -\frac{GM_p}{r^2} + \Omega^2 r (f \sin^2 \theta - 1), \quad (4)$$

$$a_\theta = -\frac{1}{r} \frac{\partial U}{\partial \theta} = f \Omega^2 r \sin \theta \cos \theta \quad (5)$$

$$a_\phi = -\frac{1}{r \sin \theta} \frac{\partial U}{\partial \phi} = -3 \Omega^2 r \sin \theta \sin \phi \cos \phi. \quad (6)$$

The vector acceleration  $\mathbf{a}$  should not be confused with the sound speed  $a$ . If we denote the coordinate along the star-planet line  $x = r \sin \theta \cos \phi$ , and normal to the orbit plane  $z = r \cos \theta$ , then the tidal force is outward when  $3x^2 > z^2$ , i.e. within latitudes  $-\pi/3$  to  $\pi/3$  of the

equator. The tidal force is zero in the  $y$ -direction. Hence when observing a planet in the plane of the sky during transit, the tidal forces are inward along  $\mathbf{e}_z$ , zero along  $\mathbf{e}_y$ , and away from the planet along  $\mathbf{e}_x$ , the line of sight during transit.

The L1 and L2 Lagrangian points at radii  $r_{L1}$  and  $r_{L2}$  are found by using eq.4 along the star-planet line ( $\theta = \pi/2, \phi = 0$ ), giving

$$r_{L1} \simeq r_{L2} \simeq r_L \equiv D (M_p/3M_*)^{1/3} = (GM_p/3\Omega^2)^{1/3} (7)$$

The near equality  $r_{L1} \simeq r_{L2}$  is due to  $M_p/M_* \ll 1$  in eq.7. The photospheres of the observed planets are inside the L1-L2 radii.

How does the magnetic field alter the radius beyond which the net gravity points outward? What is needed is the projection  $a_{\parallel} = \mathbf{a} \cdot \mathbf{b}$  along field lines, where  $\mathbf{b} = \mathbf{B}/B$  is the unit vector along the magnetic field direction. In dipole geometry, approximately correct near the planet,

$$\mathbf{B} = B_0 \left(\frac{R}{r}\right)^3 \left(\mathbf{e}_r \cos \theta + \mathbf{e}_\theta \frac{\sin \theta}{2}\right). \quad (8)$$

and the unit vector is

$$\mathbf{b} = \frac{1}{N} \left(\mathbf{e}_r \cos \theta + \mathbf{e}_\theta \frac{\sin \theta}{2}\right) \quad (9)$$

where the normalization factor is

$$N = \sqrt{\cos^2 \theta + \sin^2 \theta/4} = \sqrt{1 - 3 \sin^2 \theta/4}. \quad (10)$$

The parallel acceleration is then

$$a_{\parallel} = -\mathbf{b} \cdot \nabla U = \frac{\cos \theta}{N} \left[ -\left(\frac{GM_p}{r^2} + \Omega^2 r\right) + \frac{3}{2} f \Omega^2 r \sin^2 \theta \right] \quad (11)$$

The quantity in brackets in eq.11 must be positive in order for the net acceleration to be away from the planet. To solve for the radius at which the net acceleration is zero, we express  $\theta$  in terms of  $r$  along dipole field lines using

$$r(\theta) = R \frac{\sin^2 \theta}{\sin^2 \theta_b} \equiv r_{\text{eq}} \sin^2 \theta \quad (12)$$

where

$$r_{\text{eq}} = R / \sin^2 \theta_b \quad (13)$$

is the equatorial radius of the field line with footpoint at  $\theta_b$ . The “magnetic Roche lobe radius”,  $r_{\text{RB}}$ , at which the projected acceleration  $a_{\parallel} = 0$  is given by the solution of the equation

$$\frac{GM_p}{r_{\text{RB}}^2} + \Omega^2 r_{\text{RB}} = \frac{3}{2} f \Omega^2 \frac{r_{\text{RB}}^2}{r_{\text{eq}}}. \quad (14)$$

Solutions can only exist in the range of radii  $2r_{\text{eq}}/3f \leq r_{\text{RB}} \leq r_{\text{eq}}$ . Solutions for  $r_{\text{RB}}$  exist first at the looptop  $r_{\text{RB}} = r_{\text{eq}}$  for loops of critical size

$$r_{\text{eq,crit}} = \frac{r_L}{(f/2 - 1/3)^{1/3}}. \quad (15)$$

That is, when the loop size becomes larger than about the L1-L2 distance, the outer part of the loop can have net acceleration pointing away from the planet. Note that this statement applies even in the plane where  $\cos^2 \phi = 0$ ,

where the radial component of the tidal force points inward. The magnetic geometry allows a “magnetic Roche lobe”  $r_{\text{RB}} \sim r_{\text{R}}$  to exist at all longitudes, in contrast to the unmagnetized case.

In the next section we model the gas density in the dead zone.

## 6. THE DEAD ZONE

The 3D MHD wind equations are presented in Appendix A. There we derive the Bernoulli constant along field lines and discuss how gas pressure discontinuities at the dead zone - wind zone boundaries give rise to current sheets which alter the magnetic field configuration. For the present section which discusses the dead zone, the main concept needed is that hydrostatic balance applies along field lines. We will approximate the field lines as dipolar.

In the dead zone, the velocity along field lines  $\mathbf{v} = 0$ . Setting  $\mathbf{v} = 0$  in eq.A2 and dotting this equation with  $\mathbf{b}$  to eliminate the Lorentz force we find the equation of hydrostatic balance along field lines

$$\frac{1}{\rho} \frac{dP}{ds} = a^2 \frac{d \ln \rho}{ds} = -\frac{dU}{ds} \quad (16)$$

where  $d/ds = \mathbf{b} \cdot \nabla$  is the derivative along field lines. Under the isothermal assumption, eq.16 can then be integrated to give the run of pressure and density along a field line with base position  $(\theta_b, \phi)$ :

$$\begin{aligned} \frac{P(r, \theta, \phi)}{P(R, \theta_b, \phi)} &= \frac{\rho(r, \theta, \phi)}{\rho(R, \theta_b, \phi)} \\ &= \exp \left[ - \left( \frac{U(r, \theta, \phi) - U(R, \theta_b, \phi)}{a^2} \right) \right]. \end{aligned} \quad (17)$$

We treat the density and pressure at the base as being along equipotentials. Defining  $\rho_{ss} = P_{ss}/a^2 = \rho(r = R, \theta = \pi/2, \phi = 0)$  to be the value at the substellar point at the base radius, the density at the base radius at other points is

$$\rho_b(\theta_b, \phi) = \rho_{ss} \exp \left[ - \left( \frac{U(R, \theta_b, \phi) - U(R, \pi/2, 0)}{a^2} \right) \right] \quad (18)$$

Combining eq.17 and 18 then gives

$$\begin{aligned} \frac{P(r, \theta, \phi)}{P_{ss}} &= \frac{\rho(r, \theta, \phi)}{\rho_{ss}} \\ &= \exp \left[ - \left( \frac{U(r, \theta, \phi) - U(R, \pi/2, 0)}{a^2} \right) \right]. \end{aligned} \quad (19)$$

Note that because we have assumed the density and pressure surfaces at the base are along equipotentials, eq.19 satisfies

$$0 = -\nabla P - \rho \nabla U \quad (20)$$

in all three directions, not just along field lines. In this case  $-\nabla U$  is balanced by gas pressure forces due to a non-spherical distribution of mass. If, on the other hand, temperature, density or pressure surfaces were not along equipotentials, then eq.20 would not be satisfied perpendicular to field lines, and the trans-field force balance (eq.A12) would be required to understand the required currents.

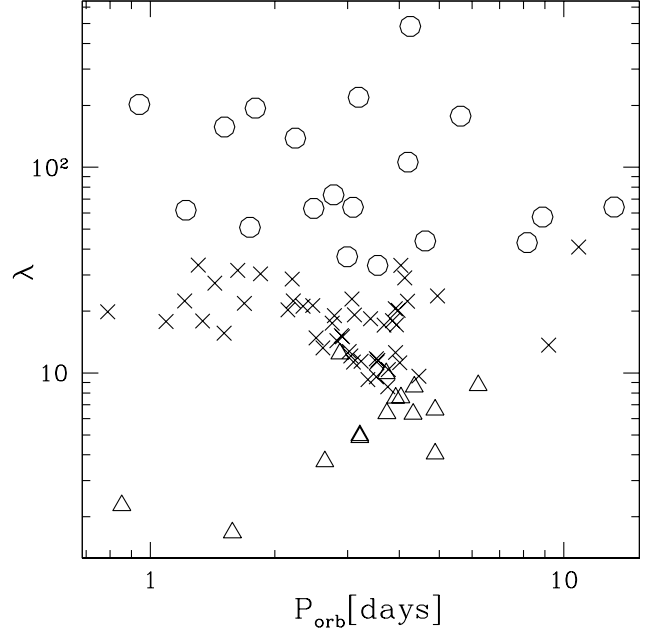


FIG. 2.— Values of  $\lambda$  calculated using eq.22 for the current database of transiting exoplanets. The parameters used are  $a = 9.3 \text{ km s}^{-1}$ , appropriate to  $T = 10^4 \text{ K}$ ,  $\mu = 1$ , and  $R = R_{\text{ph}}$ . The open circles, X’s and open triangles are planets with  $M_p/M_J > 2$ ,  $1/2 \leq M_p/M_J \leq 2$  and  $M_p/M_J < 1/2$ , respectively. Values of  $P_{\text{orb}}$ ,  $M_p$  and  $R_{\text{ph}}$  are taken from the current database of transiting exoplanets (<http://exoplanet.eu/>).

The potential difference in eq.19 can be written in dimensionless form

$$\begin{aligned} \frac{U(r, \theta, \phi) - U(R, \pi/2, 0)}{a^2} \\ = \lambda \left( 1 - \frac{R}{r} \right) + \frac{1}{2} \epsilon \left[ 3 - \left( \frac{r}{R} \right)^2 (f \sin^2 \theta - 1) \right] \end{aligned} \quad (21)$$

where we have defined the ratio of escape to thermal speed

$$\begin{aligned} \lambda &= \frac{GM_p}{Ra^2} \\ &\simeq 9.3 \left( \frac{M_p}{0.7M_J} \right) \left( \frac{1.4R_J}{R} \right) \left( \frac{10 \text{ km s}^{-1}}{a} \right)^2 \end{aligned} \quad (22)$$

and the ratio of rotation speed (or tidal potential) to thermal speed

$$\begin{aligned} \epsilon &= \left( \frac{\Omega R}{a} \right)^2 \\ &= 0.043 \left( \frac{3.5 \text{ days}}{P_{\text{orb}}} \right)^2 \left( \frac{R}{1.4R_J} \right)^2 \left( \frac{10 \text{ km s}^{-1}}{a} \right)^2 \end{aligned} \quad (23)$$

The photoionization model in section 8 shows outward increase in  $T$  and decrease in  $\mu$ , implying larger  $a$  with radius. The density will then decrease more slowly than in the isothermal model for the same quantities at the base.

Figures 2 and 3 show the values of  $\lambda$  and  $\epsilon$  versus planet orbital period for the transiting exoplanets, taking  $M_p$ , transit radius  $R_{\text{ph}}$  and orbital period  $P_{\text{orb}} = 2\pi/\Omega$  from

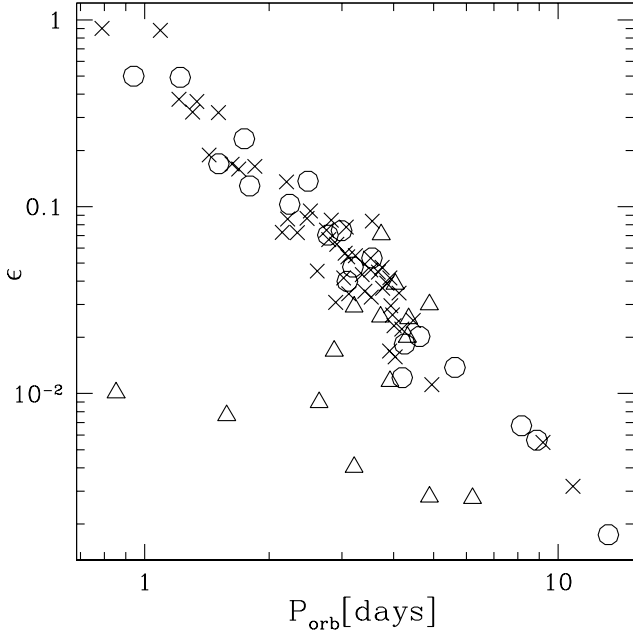


FIG. 3.— Values of  $\epsilon$  calculated using eq.23 for the current database of transiting exoplanets (<http://exoplanet.eu/>). The open circles, X's and open triangles are planets with  $M_p/M_J > 2$ ,  $1/2 \leq M_p/M_J \leq 2$  and  $M_p/M_J < 1/2$ , respectively. The parameters used are  $a = 9.3 \text{ km s}^{-1}$ , appropriate to  $T = 10^4 \text{ K}$ ,  $\mu = 1$ , and  $R = R_{\text{ph}}$ .

the Extrasolar Planets Encyclopedia<sup>4</sup>. The temperature and mean molecular weight have been set to fiducial values of  $\mu = 1$  and temperature  $T = 10^4 \text{ K}$ , giving sound speed of  $a = 9.3 \text{ km s}^{-1}$ .

Note that a substantial number of planets have  $\lambda = 2-10$ , implying the scale height of the gas is large enough that the density decrease in the dead zone is only by a factor of  $10-10^4$ , far less than for planets with cold upper atmospheres more distant from their parent star. This increased density leads to the possibility that hot Jupiter upper atmospheres may be collisional to large distances from the planet, i.e. that the exobase, if it exists at all, is at radii  $r \gg R_{\text{ph}}$  (Tian et al. 2005; Murray-Clay et al. 2009).

Next, note that for the same fiducial molecular weight and temperature, the strength of the tide,  $\epsilon$ , is in the range  $0.1-1$  for a substantial number of planets. For large  $\epsilon$ , the typical rotational speed of a synchronized planet is comparable to the sound speed, or equivalently, the free fall speed in the tidal potential is comparable to the sound speed. Since  $\epsilon$  is evaluated at the base, the tidal force will dominate even more at larger distances from the planet.

Figure 4 shows the run of gas and magnetic pressure along the equator ( $\theta = \pi/2$ ) as a function of radius along the star-planet line ( $\phi = 0$ ). Eq.19 was used for the gas pressure, and eq.8 for the magnetic pressure. The magnetic pressure is parametrized by the plasma  $\beta$  at the substellar point at the base:

$$\beta \equiv \frac{8\pi P_{ss}}{(B_0/2)^2} = 0.14 \left( \frac{P_{ss}}{0.1 \mu\text{bar}} \right) \left( \frac{B_{J,\text{eq}}}{B_0/2} \right)^2. \quad (24)$$

<sup>4</sup> <http://exoplanet.eu/>

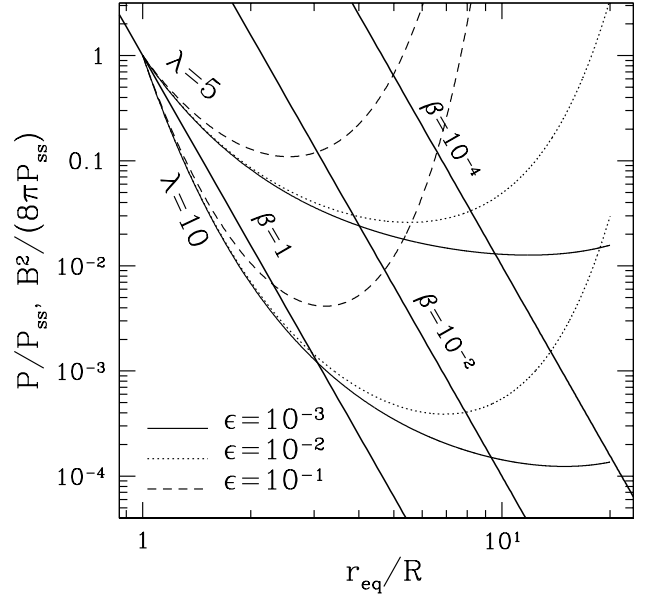


FIG. 4.— Gas and magnetic pressure, normalized to the base gas pressure  $P_{ss} = P(R, \pi/2, 0)$ , as a function of equatorial radius  $r_{\text{eq}}$  for the isothermal model. The tidal potential is evaluated along the star-planet line  $\cos^2 \phi = 1$  at the equator  $\theta = \pi/2$ . The two groups of lines starting from  $r = R$  and  $P = P_{ss}$  are  $P(r_{\text{eq}}, \pi/2, 0)/P_{ss}$  evaluated for  $\lambda = 5, 10$ . For each group, the line style gives the value of  $\epsilon$ . The three lines sloping down to the right are  $B^2(r_{\text{eq}}, \pi/2, 0)/(8\pi P_{ss}) = (R/r_{\text{eq}})^6/\beta$  for the three different values of equatorial  $\beta = 10^{-4}, 10^{-2}, 1$ . The cusp radius in Figure 5 is given by the intersection of the gas and magnetic pressure curves. The gas pressure decreases outward faster for larger  $\lambda$ . Beyond the Roche radius, gravity effectively points outward and the gas pressure begins to increase outward. For larger  $\epsilon$ , the Roche radius moves inward.

The different lines in Figure 4 show gas pressure and magnetic pressure for different  $\lambda$ ,  $\epsilon$ , and  $\beta$  as a function of radius.

For small  $\epsilon$ , the density decreases outward, and eventually becomes a constant. When the tidal force is included the density *increases* outward for radii outside the magnetic Roche radius (eq.14), since the sign of gravity points outward there. This is a dramatic effect for close-in planets, whose Roche radii are at only a few planetary radii, and may lead to hydrogen densities orders of magnitude larger than the  $\epsilon = 0$  case. The tidal gravity plays a role similar to the centrifugal force in models of the closed field line regions in the solar wind (Mestel & Spruit 1987) and in Jupiter's magnetosphere outside the corotation radius. To specify the current and field distributions required for this support involves a solution of the trans-field equation, which is beyond the scope of this work. However, such support should be possible when magnetic pressure dominates gas pressure.

Next, we follow Mestel (1968) and Mestel & Spruit (1987) to estimate the size of the dead and wind zones. Pneuman & Kopp (1971) showed that the dead zone ends at the equator in a cusp, i.e. the field in the dead zone approaches zero toward the cusp. Also, for  $v \gtrsim a$ , the wind zone pressure can be neglected compared to the dead zone pressure, leading to the condition (also see our

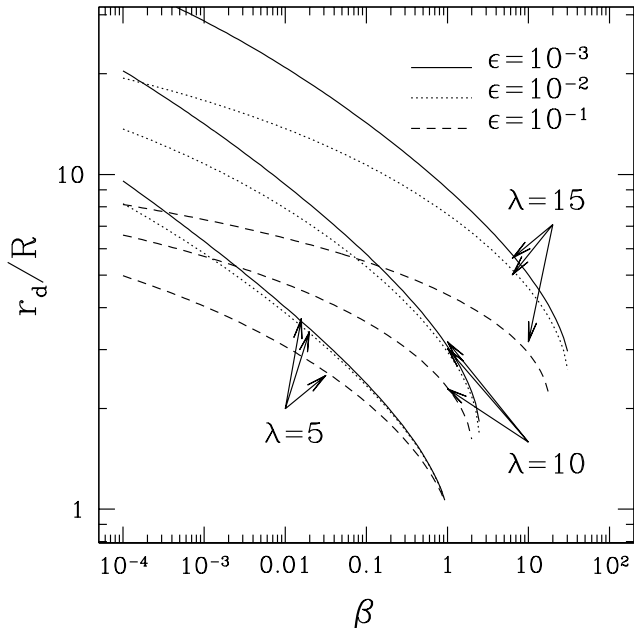


FIG. 5.— Cusp radius as a function of equatorial plasma  $\beta$  at the substellar base of the atmosphere for different values of  $\lambda = GM_p/(Ra^2)$  and  $\epsilon = (\Omega R/a)^2$ . Here  $\lambda$  is roughly the ratio of escape speed to isothermal sound speed, and  $\epsilon$  is the roughly the ratio of rotation speed to isothermal sound speed. Larger  $\lambda$  ( $\epsilon$ ) implies the density decreases outward faster (slower). The cusp radius moves outward (inward) for larger  $\lambda$  ( $\epsilon$ ).

discussion leading up to eq.A14 in Appendix A)

$$P_{\text{dead}} \simeq \frac{B_{\text{wind}}^2}{8\pi}. \quad (25)$$

To determine the cusp radius, which we call  $r_d$  for dead zone, we use eq.19 for the left hand side and eq.8 for the right hand side. The resulting equation is

$$\beta \exp \left[ -\lambda \left( 1 - \frac{R}{r} \right) + \frac{3}{2} \epsilon \left( \frac{r^2}{R^2} \cos^2 \phi - 1 \right) \right] = \left( \frac{R}{r} \right)^{-6} \quad (26)$$

Eq.26 shows that the cusp radius will depend on  $\phi$  in general due to the tidal potential. When tides can be ignored ( $\epsilon \ll 1$ ), a reasonable approximation is  $r_d/R \simeq (\epsilon^\lambda/\beta)^{1/6}$ .

Figure 5 shows cusp radii as a function of  $\beta$  for different tidal strength ( $\epsilon$ ) and binding parameter ( $\lambda$ ). Consider the fiducial case with  $\epsilon = 10^{-3}$ ,  $\lambda = 10$  and  $\beta = 10^{-2}$ . Initially the magnetic pressure is much larger than the gas pressure. The more rapid decrease of magnetic pressure implies equality at the cusp radius,  $r_d/R \simeq 10$ . Increasing  $\epsilon$ , the gas pressure is larger and the cusp radius moves inward. The cusp radius moves outward with increasing magnetic field, i.e. decreasing  $\beta$ .

Under what conditions does a magnetosphere not form? Inspection of the  $\beta = 1$  and  $\lambda = 5$  curves in Figure 4 shows that the magnetic and gas pressures are initially equal at the base, but the gas density decreases more slowly and so the magnetic field never dominates. Ignoring tides, there is an analytic criterion for the critical  $\beta_{\text{crit}} = \beta_{\text{crit}}(\lambda)$  for the formation of a dead zone. This criterion is found by requiring simultaneously  $P = B^2/8\pi$  and  $dP/dr = d/dr(B^2/8\pi)$ , and yields

$\beta \leq \beta_{\text{crit}} = (6/\lambda)^6 \exp(\lambda - 6)$ . For  $\lambda = 5, 10, 15$ , the values are  $\beta_{\text{crit}} = 1.1, 2.5$  and  $33$ , agreeing with the cutoffs in Figure 5. Hence for large  $\lambda$ , the gas at the base need not be magnetically dominated in order for the gas well above to base to become so.

In summary, we have found cusp, or dead zone, radii in the range of a few to tens of radii  $R$  for the expected range of  $\lambda$ ,  $\beta$  and  $\epsilon$ . Since transit observations to date probe the high density gas within a few planetary radii, these observations may be probing static gas trapped within the magnetosphere, as opposed to outflowing gas.

Nevertheless, as we will argue in section 7, a wind zone should exist, and we investigate its structure in the next section.

## 7. THE WIND ZONE

In this section we show how the (slow magneto-) sonic point is affected by the magnetic geometry. Readers unfamiliar with the MHD wind equations can consult Appendix A for a brief summary of the equations. We simplify the problem by assuming that the sonic point is close enough to the planet for magnetic stresses to dominate over hydrodynamic stresses — the rigid field line approximation. In this situation the fluid nearly corotates with the planet, and can be accelerated like “beads on a wire” by the magnetic field. This “magneto-centrifugal” effect from stellar wind theory (Mestel 1968) becomes important when the rotation velocity approaches the sound speed at the sonic point (Mestel & Spruit 1987). For a synchronized hot Jupiter, tidal forces are of comparable size as centrifugal forces, and the condition that the rotation velocity is comparable to the sound velocity at the sonic point is equivalent to the Roche-lobe radius being near the sonic point. The rigid field line assumption will typically break down near the Alfvén point, which we estimate lies well outside the dead zone radius for most latitudes.

Plugging parallel velocity,  $\mathbf{v} = v\mathbf{b}$ , and the no monopoles condition, eq.A7, into eq.A1, the continuity equation assumes the simple form

$$\mathbf{B} \cdot \nabla \left( \frac{\rho v}{B} \right) = 0 \quad (27)$$

so that  $\rho v/B$  is constant on field lines, and has the interpretation of the mass loss rate per unit of magnetic flux along a flux tube of area  $\propto B^{-1}$ . Similarly, the projection of eq.A2 along the field can be rewritten as

$$v \frac{dv}{ds} = -a^2 \frac{d \ln \rho}{ds} - \frac{dU}{ds}, \quad (28)$$

which has the Bernoulli integral along field lines (see eq.A8 and A9). Again, the  $(\mathbf{J} \times \mathbf{B})$  force cancels out since  $\mathbf{v} \parallel \mathbf{B}$ . Combining eq.27 and 28 gives the momentum equation parallel to field lines:

$$\left( v - \frac{a^2}{v} \right) \frac{dv}{ds} = -a^2 \frac{d \ln B}{ds} - \frac{dU}{ds}. \quad (29)$$

At the critical point,  $v = a$ , and hence to avoid a divergent acceleration, the right hand side must go to zero, giving

$$-a^2 \frac{d \ln B}{ds} = \frac{dU}{ds} \quad (30)$$



at the sonic point. The term on the left hand side represents the pressure gradient due to the geometry set by the magnetic field. The term on the right hand side is the net acceleration along the field line.

Since the sonic point is sufficiently close to the surface that the field geometry is not much perturbed by external currents, we use dipole geometry to evaluate the sonic point position. The dipole field in eq.8 gives the intermediate result

$$-\frac{d \ln B}{ds} = \frac{3 \cos \theta}{Nr} \left( 1 + \frac{\sin^2 \theta}{8N} \right). \quad (31)$$

The two terms on the right hand side of eq.31 represent the field line divergence due to the  $r^{-3}$  factor from dipole field geometry, and the  $\theta$ -dependent factor  $N$ . The term due to differentiating  $N$  is negligible for large loops, but becomes important for small loops near the equator. Plugging eq.11 and 31 into eq.30, and eliminating  $\theta$  using the field line geometry in eq.12, we find the following equation to determine the sonic point  $r = r_s$ :

$$\frac{GM_p}{r^2} + \Omega^2 r = \frac{3a^2}{r} \quad (32)$$

where  $N = \sqrt{1 - 3r/4r_{\text{eq}}}$ . This equation, solely in terms of  $r$ , can be solved as a function of the parameters  $\lambda$ ,  $\epsilon$  and  $r_{\text{eq}}/R = 1/\sin^2 \theta_b$ .

First we examine the limit in which tidal forces can be neglected. This simple case highlights the importance of the magnetic field geometry, and would apply for slow rotating planets distant from the star. Setting  $\Omega = 0$  in eq.32, the simpler equation

$$\frac{GM_p}{3a^2 r} = 1 + \frac{r}{8r_{\text{eq}} \sqrt{1 - 3r/4r_{\text{eq}}}} \quad (33)$$

results. For large field lines  $r_{\text{eq}} \gg R$ , field line curvature is negligible and the sonic point sits at

$$r_{s0} \simeq \frac{GM_p}{3a^2} = \left( \frac{\lambda}{3} \right) R \quad (34)$$

which differs from the spherical wind result by the 3, instead of 2, in the denominator. Including finite  $\sin^2 \theta_b$ , the sonic point moves inward somewhat.

Next, we include tidal forces, but ignore the field line curvature terms on the right hand side scaling as  $r_{\text{eq}}^{-1}$ , a good approximation for field lines near the pole. This approximation eliminates the possibility that the tidal force can point outward. In this case, the sonic point equation becomes

$$\frac{GM_p}{r^2} + \Omega^2 r = \frac{3a^2}{r}. \quad (35)$$

The key point is that now the effective gravity on the left hand side has a *minimum*. If the pressure term on the right hand side is smaller than this minimum, a transonic solution is not possible. The solution of the cubic eq.35 lying near the planet disappears for sufficiently strong tidal forces

$$\begin{aligned} \Omega &\geq \Omega_{\text{crit}} = 2 \frac{a^3}{GM_p} = \frac{2}{3} \frac{a}{r_{s0}} \\ &= \left( \frac{2\pi}{3.4 \text{ days}} \right) \left( \frac{0.7 M_J}{M_p} \right) \left( \frac{a}{10 \text{ km s}^{-1}} \right)^3. \end{aligned} \quad (36)$$

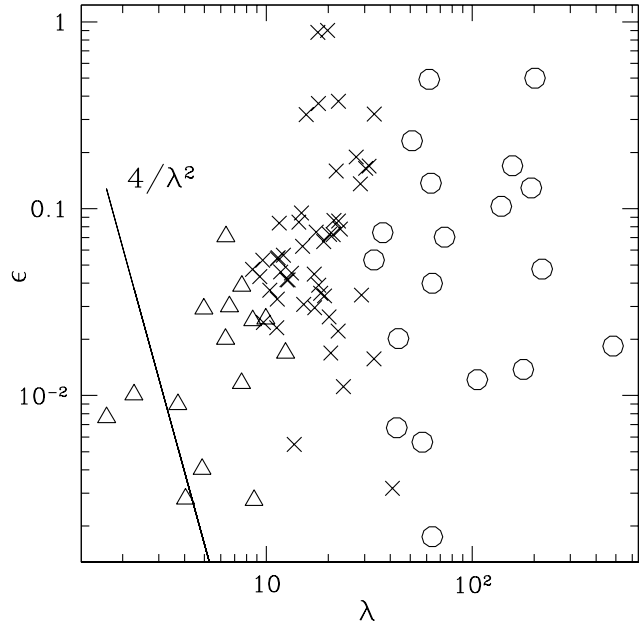


FIG. 6.— Values of  $\epsilon$  versus  $\lambda$  for the transiting planets. The points are the data, with symbol type as in Figures 2 and 3. The line is the critical tidal strength  $\epsilon = 4/\lambda^2$  above which the wind is suppressed in the polar region. We have used  $a = 9.3 \text{ km s}^{-1}$  to make the plot.

Eq.36 can also be written in dimensionless form as

$$\epsilon_{\text{crit}} = \frac{4}{\lambda^2}. \quad (37)$$

When eq.36 is satisfied, for planets sufficiently close to the star, there is no sonic point solution, and the wind is shut off near the poles. The density distribution on these field lines will be hydrostatic. Hence, for sufficiently strong tides such that the rotation velocity  $\Omega_{\text{crit}} r_{s0}$  at the sonic point is supersonic, a second dead zone is created in the polar regions where tides point inward. Whereas the first dead zone in the equatorial region is due to magnetic pressure dominating gas pressure, the second dead zone near the poles arises due to the large potential barrier.

Figure 6 shows  $\epsilon$  versus  $\lambda$  for the observed transiting planets. Except for a handful of planets with the smallest values of both  $\epsilon$  and  $\lambda$ , most of the planets are in the strong tide limit with  $\epsilon > \epsilon_{\text{crit}}$ . The planets in the upper right hand corner will have the polar wind partially shut off, while the planets in the lower left hand corner will be able to drive a polar wind.

Next, we retain the  $r_{\text{eq}}^{-1}$  terms due to the tidal force in eq.32. Taking the limit  $\Omega \rightarrow \infty$  in eq.32, the sonic point in the strong tide limit is

$$r_s \rightarrow \frac{2r_{\text{eq}}}{3f}. \quad (38)$$

In this limit, the sonic point occurs at a fixed fraction of the loop equatorial radius, dependent only on  $\cos^2 \phi$ , and agrees with the magnetic Roche lobe radius found in eq.14, where the net force first points outward.

Figure 7 shows an example numerical solution of eq.32 for the sonic point radius as a function of footpoint angle  $\theta_b$ . Dipole geometry was used to produce this plot. In the weak tide limit ( $\epsilon \rightarrow 0$ ), the solutions asymptote

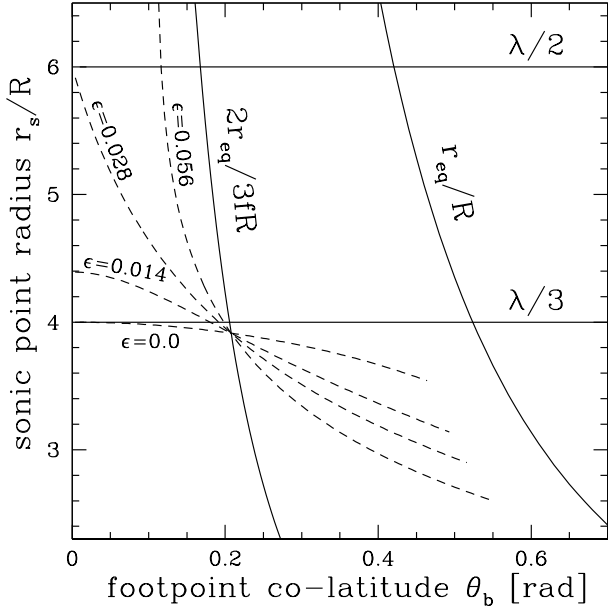


FIG. 7.— Sonic point radius as a function of footpoint co-latitude for  $\lambda = 12$ ,  $\beta = 1$  and a range of  $\epsilon$  (dashed lines). The three solid lines label the  $\epsilon = 0$  sonic point,  $r_{s0}/R = \lambda/3$ , the  $\epsilon = 4/\lambda^2 = 0.16$  sonic point,  $r_s/R = \lambda/2$ , and the  $\epsilon = \infty$  sonic point,  $r_s = 2r_{\text{eq}}/3f$ . Each dashed line terminates at large  $\theta$  at the dead zone,  $\theta = \theta_d$ . The dead zone shrinks ( $\theta_d \rightarrow \pi/2$ ) as  $\epsilon$  increases. The value of  $\beta$  is needed only for the size of the dead zone. The longitude  $\cos^2 \phi = 1$ , along the star-planet line, has been assumed here.

to eq.34 for large loop size, and decrease slightly before terminating at the dead zone,  $\theta = \theta_d$ . For small  $\epsilon \lesssim 4/\lambda^2$ , the sonic point moves out in the polar regions, and inward closer to the equator; the dividing line between these two behaviors depends on if the net force is outward or inward near the looptop. Next, for the critical value  $\epsilon = 4/\lambda^2$ , the sonic point is at roughly  $r_s \simeq (\lambda/2)R$  near the pole. For larger values  $\epsilon \gtrsim 4/\lambda^2$ , the sonic point near the pole jumps out to a radius much further from the planet, near  $r_s \sim 2r_{\text{eq}}/3f$ , where the net gravity changes sign. For small values of  $\theta_b$ , this solution may be at tens to hundreds of planetary radii, and is of no physical interest. Physically, when the sonic point moves outside the region of interest the field line is effectively hydrostatic.

Figure 8 shows the velocity at the base,  $v_b$ , for the same parameters as in Figure 7. This velocity was found by using the Bernoulli constant evaluated at the sonic point and the base. For weak tides ( $\epsilon = 0$ ), the velocity at the base is nearly constant over the wind zone. As  $\epsilon$  increases, the base velocity decreases near the pole, where the sonic point has moved outward, and increases closer to the equator, where the sonic point has moved inward.

At sufficiently large radii, pressure gradients rapidly become negligible and the fluid should move on a nearly ballistic trajectory. Using the Bernoulli integral defined in eq.A9, with the sonic point as reference location, the velocity parallel to the magnetic field is

$$v^2 = a^2 + 2a^2 \ln \left( \frac{B_s v}{B a} \right) + 2(U_s - U) \quad (39)$$

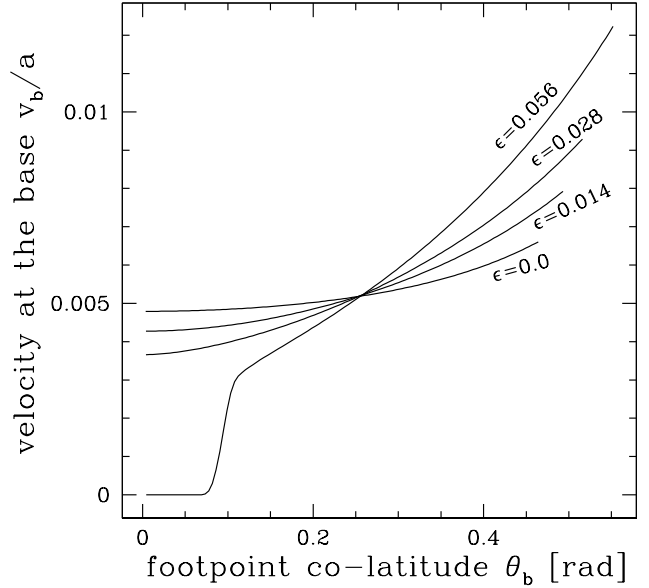


FIG. 8.— Velocity at the base, in units of  $a$ , for the same parameters as Figure 7.

where the subscript “s” refers to the sonic point. The transit signal depends only on the gas velocity within the stellar disk at  $r \leq R_*$ , where  $R_*$  is the stellar radius. The tidal potential term  $-2U$  dominates at large radius. For the purposes of a simple estimate, this asymptotic expression, evaluated at the stellar radius, gives

$$\begin{aligned} v_{\text{asympt}} &\simeq \Omega R_* (f \sin^2 \theta - 1)^{1/2} \\ &= 24 \text{ km s}^{-1} \left( \frac{3.6 \text{ day}}{P_{\text{orb}}} \right) \left( \frac{R_*}{R_{\odot}} \right) \left( \frac{f \sin^2 \theta - 1}{3} \right)^{1/2} \end{aligned} \quad (40)$$

We caution the reader that the (logarithmic) enthalpy term in eq.39 is not negligible, and can increase the velocity at  $r = R_*$  by a factor of order 2 (see Figure 11). Though supersonic, the velocity in eq.40 is much smaller than the  $\sim \pm 100 \text{ km s}^{-1}$  at which absorption is observed in the Lyman  $\alpha$  spectrum of HD 209458b (Vidal-Madjar et al. 2003), and hence velocity gradients cannot be the origin of the observed transit depth.

In the following sections, we will implement the general theory that describes the structure of the dead zone (§ 6) and of the wind zone (§ 7) to construct global models of hot Jupiter magnetospheres for comparison with transit observations of HD 209458b. A simplified 1D thermal model motivates our choice of the pressure and sound speed at the base of the global models, which are key parameters for determining the magnetospheric structure.

## 8. THE H AND H<sup>+</sup> LAYERS: A SIMPLIFIED 1D THERMAL MODEL

The thickness of the warm H layer with temperature  $T \simeq 5,000 - 10,000 \text{ K}$  is a crucial parameter in determining the transit depth, as emphasized in the phenomenological model of Koskinen et al. (2010) (see García Muñoz (2007) for a discussion of the role of base pressure for an atmosphere undergoing energy-limited escape). The large temperature and small mean molecular

weight increase the scale height to  $\sim 0.1R_{\text{ph}}$ . If the warm layer extends over  $\gtrsim 10$  scale heights, the transit radius can be significantly increased over the photospheric radius of the optical continuum. In this section, we construct a simple 1D model in photoionization and thermal equilibrium to determine the depth of the warm H layer.

At sufficiently low density and temperature, the rates of collisional ionization and 3-body recombination are slow compared to photoionization and radiative recombination, respectively, and the ionization state is set by a balance of the latter two processes. We consider a pure hydrogen gas for simplicity. Let  $n_e$ ,  $n_p$  and  $n_H$  be the density of electrons, protons and hydrogen atoms. Charge neutrality implies  $n_e = n_p$ . The ionization fraction in the ‘‘on the spot’’ approximation is found by solving the algebraic equation (Osterbrock & Ferland 2006)

$$n_H J(N_H) = \alpha_B(T) n_e n_p = \alpha_B(T) n_p^2. \quad (41)$$

At the 50% ionization point,

$$n_H = n_p \equiv n_{\text{eq}} = \frac{J}{\alpha_B}. \quad (42)$$

Here  $\alpha_B(T) \simeq 2.6 \times 10^{-13} \text{ cm}^3 \text{ s}^{-1} (10^4 \text{ K}/T)^{0.8}$  is the case B radiative recombination rate (Osterbrock & Ferland 2006),

$$J(N_H) = \int_{\nu_0}^{\infty} d\nu \varphi_{\nu} e^{-N_H \sigma_{\text{pi}}(\nu)} \sigma_{\text{pi}}(\nu) \quad (43)$$

is the photoionization rate per H atom,  $\varphi_{\nu}$  is the photon flux per unit frequency interval,  $N_H$  is the atomic hydrogen column from the point in question to the star,  $\sigma_{\text{pi}}(\nu) = \sigma_{\text{pi}}(\nu_0/\nu)^3$  is the H atom bound-free cross section, the threshold cross section is  $\sigma_{\text{pi}} = 6.3 \times 10^{-18} \text{ cm}^2$ , and the threshold frequency is  $\nu_0 = 13.6 \text{ eV}/h$ . The exponential factor in eq.43 takes into account attenuation of the stellar radiation. Eq.43 may be computed as a function of  $N_H$ , as described in Osterbrock & Ferland (2006).

For the thermal balance, the dominant processes are photoelectric heating from the ionization of hydrogen atoms (Yelle 2004), and cooling by collisionally excited Lyman  $\alpha$  emission from electron impacts (Murray-Clay et al. 2009). Assuming 100% efficiency of turning photoelectron energy into heat, the heating rate per reaction is

$$Q(N_H) = \int_{\nu_0}^{\infty} d\nu \varphi_{\nu} e^{-N_H \sigma_{\text{pi}}(\nu)} \sigma_{\text{pi}}(\nu) h(\nu - \nu_0) \quad (44)$$

Balancing photoelectric heating and cooling by collisionally excited Lyman  $\alpha$  emission implies

$$n_H Q(N_H) = \Lambda(T) n_e n_H. \quad (45)$$

Note that  $n_H$  cancels out of eq.45. The line cooling coefficient for Lyman  $\alpha$  is  $\Lambda(T) = 2.9 \times 10^{-19} \text{ erg cm}^3 \text{ s}^{-1} \sqrt{10^4 \text{ K}/T} \exp(-118,400 \text{ K}/T)$  (Dalgarno & McCray 1972). Increasing distance from the star and decreased heating efficiency act to decrease  $Q$ .

Eq. 41 and 45 are two algebraic equations which can be solved for  $n_H$  and  $n_p$  in terms of  $N_H$  and  $P = (2n_p + n_H)k_b T$ . In practice, we assume a trial  $T$ , compute

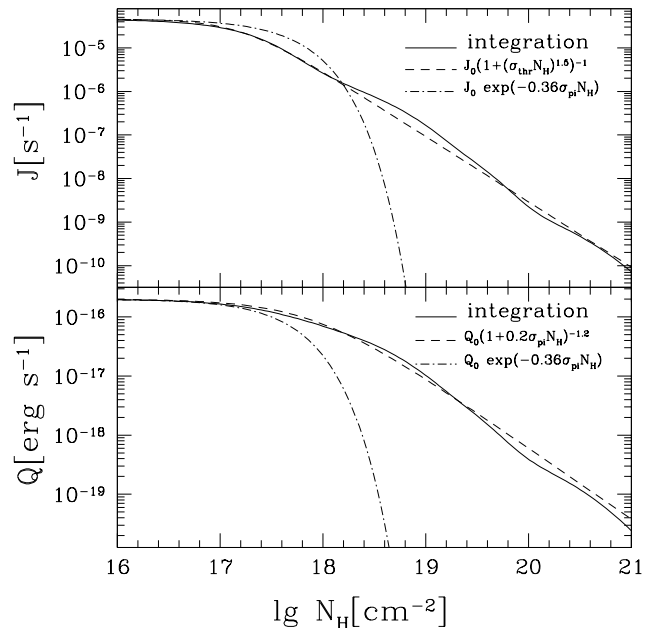


FIG. 9.— Photoionization rate (top) panel and heating rate (bottom) as a function of neutral hydrogen column, for a planet at  $D = 0.05 \text{ AU}$  around a solar-type star.

$n_H$  and  $n_p$  from eq.41, and then compute the imbalance of heating and cooling in eq.45. The temperature is iterated until thermal balance is achieved. The equations for dependent variables  $N_H$  and  $P$  and independent variable  $r$  are the definition of column

$$\frac{dN_H}{dr} = -n_H \quad (46)$$

and hydrostatic balance

$$\frac{dP}{dr} = -\frac{GM_p m_p}{r^2} (n_H + n_p), \quad (47)$$

where tides have been ignored for simplicity. The inner boundary condition is  $r = R$  at the chosen base pressure. The column  $N_H$  should go to zero at the outer boundary. We enforce this boundary condition at the finite, but large, radius  $r = 40R$ .

To compute the integrals in eq.43 and eq.44, we use the quiet solar Lyman continuum spectrum from Woods et al. (1998), which tabulates  $\int d\nu \varphi_{\nu}$  in each frequency bin. The results are shown as the solid lines in Figure 9. Approximate power-law fits are also shown, along with curves representing pure exponential attenuation for comparison. A similar fit with shallower slope is shown in the bottom panel for the heating rate  $Q(N_H)$ . At small optical depth,  $J_0 \approx 6 \text{ hr}$  and the mean photoelectron energy is  $Q_0/J_0 \simeq 2.7 \text{ eV}$ . Given the form of the integrand in eq.43, one might have expected an exponential scaling of the form  $J \propto \exp[-(\text{constant})\sigma_{\text{pi}}N_H]$ , implying negligible heating and ionization deep in the H layer. This is shown as the dot-dashed line in Figure 9, and cuts off much too sharply. The numerical result is better fit with a power-law,  $J \propto N_H^{-1.5}$ , leading to larger heating rate deep into the H layer.

The weak scaling of  $J$  with  $N_H$  can be explained as the competition between  $\exp[-N_H \sigma_{\text{pi}}(\nu)]$ , which increases to

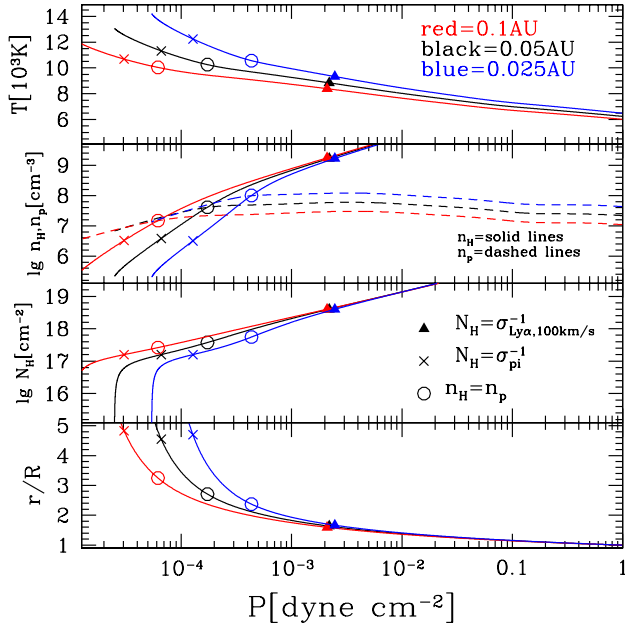


FIG. 10.— Temperature (top panel), number densities (second panel), neutral hydrogen column (third panel), and radius (bottom panel) versus pressure for a  $M_p = 0.7M_J$ ,  $R = 1.3R_J$  planet. The red, black and blue lines are for planets at  $D = 0.1, 0.05, 0.025$  AU, respectively. The hollow circles show the position where Lyman continuum radiation (at threshold) from the star becomes optically thick. The crosses show the 50% ionization point. The filled triangles show the position in the atmosphere where stellar Lyman  $\alpha$  photons at  $\pm 100$  km  $s^{-1}$  from line center become optically thick.

higher frequencies, and  $\varphi_\nu$ , which on average decreases to higher frequency. Ignoring lines in  $\varphi_\nu$ , the product of these two functions is a sharp peak, similar to the Gamow peak in thermonuclear reaction rates. For instance, if one approximates the Lyman continuum as a blackbody with temperature  $T = 8300$  K (Noyes & Kalkofen 1970), steepest descent evaluation of eq.43 gives the weak exponential scaling  $J \propto \exp[-15.9(N_H\sigma_{\text{pi}})^{1/4}]$ , which involves  $N_H^{1/4}$  in the exponent rather than  $N_H$ . However, the blackbody fit is not adequate, as even this weaker scaling cuts off too fast. We find a better fit is to use a power-law form  $\varphi_\nu \propto \nu^{-\gamma}$ , leading to  $J \propto N_H^{-(\gamma+2)/3}$ , with no exponential scaling. Choosing  $\gamma = 2.5$  then recovers the observed scaling. While these analytic scalings are useful for intuition, the solar Lyman continuum contains many strong lines, and is not well approximated by a smooth continuum function when computing  $J$ .

Figure 10 shows a numerical integration of eqs. 46, 47, 41 and 45. Spherically symmetric irradiation is assumed, the base pressure is chosen to be  $P = 1$  dyne  $\text{cm}^{-2}$ , and the  $N_H \rightarrow 0$  condition is applied at the (arbitrary) radius  $r = 40R_{\text{ph}}$ . Parameters appropriate for HD 209458b have been chosen with  $M_p = 0.7M_J$  and  $R = 1.3R_J$ . In each panel, the three different color curves are for different semi-major axis; the semi-major axis of HD 209458b is  $D \simeq 0.05$  AU. In the top panel, note that  $T$  increases slowly as the planet is moved closer to the star. A factor 16 increase in stellar flux translated into only a 10-20% increase in the pressure range of interest, due to the exponential  $T$  dependence in the cooling rate. Eq.45 can

be solved analytically as

$$T \simeq \frac{1.1 \times 10^4 \text{ K}}{1 + 0.089 \ln[(n_e/n_{\text{eq},0})(Q_0/Q)]}. \quad (48)$$

This simple estimate shows that the temperature is always near  $10^4$  K near the base of the photoionized layer where  $n_H = n_p \simeq n_{\text{eq}}$ . As  $n_e$  decreases below  $n_{\text{eq}}$ , the temperature rises logarithmically slowly. This temperature rise toward small density will increase the scale height and density at larger radii relative to an isothermal model with the same base conditions.

The second panel shows the rapid inward increase of  $n_H$ , with a change in slope at the H-H<sup>+</sup> boundary. The slow decrease of  $n_p$  into the atmosphere is due to the slow decrease of  $J$  with  $N_H$ . If we had used the exponential scaling  $J \propto \exp(-N_H\sigma_{\text{pi}})$  shown in Figure 9,  $T$  and  $n_p$  would have decreased inward much more rapidly. The hollow circles show the position of  $n_H = n_p$  at each  $D$ . Planets further from the star remain neutral higher up in the atmosphere.

The third panel shows  $N_H$ , and x's show the position of  $N_H\sigma_{\text{pi}} = 1$ , where the Lyman continuum at threshold is optically thick. The optical depth unity point moves to lower pressure for planets more distant from the star, although the radius at this point is relatively constant.

The bottom panel shows radius in units of base radius. The warm H layer with temperature  $T \simeq 10,000$  K at pressures  $P = (0.1 - 100)$  nbar contributes an amount  $\simeq (1-2) \times R_{\text{ph}}$  to the radius. Specifically, even the region below  $N_H\sigma_{\text{pi}} = 1$  can be warm enough to contribute significantly to the radius. In our reference global model below, we use a base pressure  $P_{\text{ss}} = 40$  nbar (see Model 1 of Table 1).

We now discuss how the simple 1D model differs from previous investigations. One crucial difference is that the dead zone should be hotter than the wind zone, for which adiabatic expansion is an important coolant. Yelle (2004) included heating arising from photoionization of hydrogen, but ignored the attenuation of the stellar Lyman continuum into the atmosphere, leading to an overestimate of the heating rate. This attenuation of EUV in the H layer will also lead to smaller heating by H<sub>2</sub> photoionization much deeper in the atmosphere. Murray-Clay et al. (2009) included finite optical depth, but enforced an exponential cutoff which led to a steep temperature drop below the  $N_H\sigma_{\text{pi}} = 1$  point. As shown in Figure 9, the exponential cutoff is too rapid, and the slower power-law cutoff found here gives additional heating deeper in the atmosphere.

Figure 10 shows that the  $n_H = n_p$  and  $N_H\sigma_{\text{pi}} = 1$  points occur near each other at  $D = 0.05$  AU, hence attenuation due to finite optical depth cannot be ignored. The relative position of the  $n_H = n_p$  and  $N_H\sigma_{\text{pi}} = 1$  layers can be estimated as follows. The number density at which  $n_p = n_H$  is

$$n_{\text{eq}} = \frac{J}{\alpha_B} \simeq 1.8 \times 10^8 \text{ cm}^{-3} \left( \frac{T}{10^4 \text{ K}} \right)^{0.8} \left( \frac{0.05 \text{ AU}}{D} \right)^2 \left( \frac{J}{J_0} \right) \quad (49)$$

This can be converted into a pressure as

$$P_{\text{eq}} = 3k_b T n_{\text{eq}}$$

$$\begin{aligned}
&= 8.0 \times 10^{-4} \text{ dyne cm}^{-2} \left( \frac{M_p}{M_J} \right) \left( \frac{10^{10} \text{ cm}}{R} \right) \left( \frac{10}{\lambda} \right) \\
&\times \left( \frac{0.05 \text{ au}}{D} \right)^2 \left( \frac{T}{10^4 \text{ K}} \right)^{0.8} \left( \frac{J}{J_0} \right) \quad (50)
\end{aligned}$$

The  $D^{-2}$  scaling implies that the atmosphere becomes neutral out to smaller pressures as the planet moves away from the star. To estimate where  $N_H \sigma_{\text{pi}} = 1$ , we assume  $n_p \gg n_H$ ,  $P \simeq 2k_b T n_p$ , and eq.41 gives  $n_H \simeq n_p^2 / n_{\text{eq},0}$ , where  $n_{\text{eq},0} = J_0 / \alpha_B$ . For H atom scale height  $\simeq k_b T / m_p g$ , the pressure at which  $N_H \sigma_{\text{pi}} = 1$  is

$$P_{N_H \sigma_{\text{pi}}=1} \simeq 2k_b T \left( \frac{n_{\text{eq},0} m_p g}{k_b T \sigma_{\text{pi}}} \right)^{1/2} \propto D^{-1}. \quad (51)$$

The scaling with  $D$  in eq.51 implies that planets further from the star will become optically thick at lower pressure. Comparing the scalings in eq.50 and 51, one may expect 50% ionization to occur outside  $N_H \sigma_{\text{pi}} = 1$  at sufficiently large  $D$ .

Lastly, we note that since the cooling rate  $\propto n_e n_H$ , we may expect Lyman  $\alpha$  cooling to be inefficient at both high and low density, where other cooling mechanisms, such as heat conduction, may be more efficient.

## 9. GLOBAL MODELS

We now attempt to construct global models for the magnetosphere, in order to compute the planetary transmission spectrum and mass loss rates. We assume the following magnetic field model (Mestel 1968; Okamoto 1974):

$$\mathbf{B}(r, \theta) = \begin{cases} B_0 \left( \frac{R}{r} \right)^3 (e_r \cos \theta + \frac{1}{2} e_\theta \sin \theta), & (r < r_d) \\ B_0 \left( \frac{R}{r_d} \right)^3 \left( \frac{r_d}{r} \right)^2 \cos \theta e_r, & (r > r_d). \end{cases} \quad (52)$$

This global field model allows a position  $(r, \theta)$  to be associated with a base co-latitude  $\theta_b$  at  $r = R$ . The field is dipole for  $r < r_d$ , and radial outside  $r_d$ . This radial field is distinct from the split monopole due to the  $\cos \theta$  factor. Eq.52 is approximately correct for the dead zone, and also for determining the sonic point position in the wind zone if the sonic point is close to the planet. However, as ballistic trajectories with speeds far less than escape speed are expected to be bent down toward the orbital plane, the radial field assumption will be unphysical for some latitudes.

Given parameters  $\lambda$ ,  $\epsilon$ ,  $\beta$ , and longitude  $\phi$ , we first solve eq.26 for  $r_d$  using dipole geometry. For field lines inside the dead zone,  $\sin \theta_b > \sin \theta_d = \sqrt{R/r_d}$ , the velocity is zero and the density is given by the hydrostatic expression in eq.19, where  $P_{\text{ss}}$  is a model parameter. On field lines outside the dead zone,  $\sin \theta_b < \sin \theta_d = \sqrt{R/r_d}$ , we search for sonic points by looking for minima of the quantity  $-\ln(B/B_0) - U/a^2$  on field lines, between the base radius  $R$  and a chosen maximum radius  $r_{\text{max}}$ . Given the position of the sonic point  $(r_s, \theta_s)$ , the Bernoulli equation  $v^2/2 + a^2 \ln(B/v) + U = \text{constant}$  can be used to solve for the velocity at the base,  $v_b(\theta_b, \phi)$ . Given  $v_b$  and the base density (eq.18), the Bernoulli equation may again be used to find the run of  $v$  and  $\rho$  on the field line.

Detailed results will be presented for the 9 models listed in Table 1. The planetary mass and radius, and the

stellar mass and radius are characteristic of HD 209458b. We vary parameters not directly measured, such as  $P_{\text{ss}}$ ,  $a$ ,  $B_0$ , as well as the orbital radius  $D$ .

The numerical implementation of the sonic point solver deserves further discussion. Anywhere from zero to several solutions to eq.30 may be found in the interval  $R \leq r \leq r_{\text{max}}$ . Some sonic points may be spurious if a potential barrier exterior to the sonic point decelerates the flow to subsonic, even zero, speed. These spurious solutions are discarded by defining the true sonic point solution to be a *global* minimum of  $-\ln(B/B_0) - U/a^2$  which occurs *within* the interval  $R < r < r_{\text{max}}$ . If the global minimum occurs at either of the endpoints of the interval, then there is no good sonic point solution.

For minimum at the base  $r = R$ , the integration is flagged as a region of parameter space with no solution, as we should have used a base position deeper in the planet. For sonic points sufficiently deep in the planet that ram pressure dominates magnetic pressure at the sonic point, we expect the Roche lobe overflow model to be recovered. The other problem is that the global minimum can occur at the outer boundary of the integration,  $r = r_{\text{max}}$ . For instance, this can occur in the polar regions due to the upwardly increasing potential. For  $r > r_d$ , field lines with  $\sin \theta > \sin \theta_{\text{crit}} = f^{-1/2}$  have outward tidal force. Field lines with outward tidal force will have fluid accelerated outward, promoting the existence of a sonic point. The field line starting at base co-latitude  $\sin \theta_{b,\text{crit}} = (R/fr_d)^{1/2}$  will be the last field line on which the tidal force points outward. Accordingly, if no sonic point solution is found in the radial range  $R < r < r_{\text{max}}$ , and the field line has  $\sin \theta < \sin \theta_{b,\text{crit}}$ , then we treat the field line as hydrostatic and set the velocity to zero. Such field lines have outwardly increasing potential, and hence outwardly decreasing density. If, however, we had used a field line model that allowed the field at  $r > r_d$  to bend downward toward the orbital plane, it is likely that a sonic point could have been found. This affects our later numerical results, as we analytically predicted the critical tidal strength to be  $\epsilon = 4/\lambda^2$  in order to find sonic points in the polar region, whereas the above prescription would force these field lines to be hydrostatic due to the potential barrier. This approximate treatment of the polar regions likely does not affect either the total mass loss rate, or the column density profiles, since the sonic point will be so far from the planet that the velocity near the planet is quite subsonic, and the fluid will be nearly hydrostatic.

Figure 11 shows the density and speed along a particular field line in the wind zone. The change in slope near  $r = 4.7R$  is the change in field geometry at  $r = r_d$ . The speed along the field line is somewhat larger than the asymptotic result in eq.40 due to the enthalpy ( $\ln$ ) terms in eq.39. In the lower panel, the density is approximately hydrostatic inside the sonic point at  $r_s = 2.4R$ , and decreases roughly as  $\rho \propto B/v \propto r^{-3}$  outside that point. This plot explicitly demonstrates that the gas density in the wind zone can be orders of magnitude smaller than nearby gas in the dead zone, which satisfies hydrostatic balance.

Figure 12 shows contours of mass density on slices through the center of the planet in the  $y-z$  plane, as viewed during transit, and the  $x-z$  plane, as viewed mid-

TABLE 1  
GLOBAL MODELS

model #	$M_p^a$ ( $M_J$ )	$R_{ph}^b$ ( $R_J$ )	$D^c$ (AU)	$R^d$ ( $R_J$ )	$P_{ss}^e$ ( $\mu\text{bar}$ )	$a^f$ (km/s)	$B_0^g$ (G)	$\lambda^h$	$\epsilon^i$	$\beta^j$	$r_L^k$ ( $R$ )	$r_{s,0}^l$ ( $R$ )	$r_d^m$ ( $R$ )	$\delta F/F^n$	$\dot{M}^o$ (g/s)	$r_{scat}^p$ ( $R$ )
1	0.7	1.3	0.05	1.4	0.04	10.0	8.6	9.3	0.032	0.054	4.6	3.1	6.0	0.074	$9.3 \times 10^{10}$	6.6
2	0.7	1.3	0.05	1.4	0.4	10.0	8.6	9.3	0.032	0.54	4.6	3.1	3.3	0.31	$1.4 \times 10^{12}$	10.0
3	0.7	1.3	0.05	1.4	0.004	10.0	8.6	9.3	0.032	0.0054	4.6	3.1	9.7	0.025	$6.6 \times 10^9$	4.5
4	0.7	1.3	0.05	1.4	0.04	13.0	8.6	5.5	0.019	0.054	4.6	1.8	3.0	0.24	$1.7 \times 10^{12}$	9.7
5	0.7	1.3	0.05	1.4	0.04	7.5	8.6	16.6	0.056	0.054	4.6	5.5	23.2	0.030	$1.5 \times 10^8$	2.8
6	0.7	1.3	0.05	1.4	0.04	10.0	43.0	9.3	0.032	0.0022	4.6	3.1	11.6	0.091	$5.9 \times 10^{10}$	6.8
7	0.7	1.3	0.05	1.4	0.04	10.0	2.9	9.3	0.032	0.49	4.6	3.1	3.4	0.072	$1.4 \times 10^{11}$	7.8
8	0.7	1.3	0.025	1.4	0.04	10.0	8.6	9.3	0.25	0.054	2.3	3.1	6.4	0.075	$6.6 \times 10^{10}$	4.2
9	0.7	1.3	0.10	1.4	0.04	10.0	8.6	9.3	0.0040	0.054	9.2	3.1	5.9	0.096	$1.4 \times 10^{11}$	7.7

<sup>a</sup> Planet mass.

<sup>b</sup> Transit radius.

<sup>c</sup> Orbital separation.

<sup>d</sup> Radius at the base of the warm H layer.

<sup>e</sup> Pressure at base radius ( $r = R$ ) at the substellar point ( $\theta, \phi$ ) = ( $\pi/2, 0$ ).

<sup>f</sup> Isothermal sound speed.

<sup>g</sup> Magnetic field at pole ( $\theta = 0, \pi$ ) at base radius ( $r = R$ ).

<sup>h</sup>  $\lambda = GM_p/Ra^2$

<sup>i</sup>  $\epsilon = (\Omega R/a)^2$ , where  $\Omega$  is the orbital frequency.

<sup>j</sup>  $\beta = 8\pi P_{ss}/(B_0/2)^2$  is the base value at the substellar point.

<sup>k</sup> Radius of  $L_1 - L_2$  Lagrange points.

<sup>l</sup> Sonic point radius ignoring tides and field line curvature (eq.34).

<sup>m</sup> Dead zone radius in  $\phi = \pi/2$  plane.

<sup>n</sup> Integrated Lyman  $\alpha$  transit depth from  $-200$  to  $200$  km  $s^{-1}$  from line center. The disk inside the base radius is assumed opaque, and contributes  $(R/R_\star)^2 \simeq 0.015$  to the transit depth for  $R = 1.4R_J$  and  $R_\star = 1.15R_\odot$ .

<sup>o</sup> Computed mass loss rate.

<sup>p</sup> Radius  $(A_{scat}/\pi)^{1/2}$  corresponding to area  $A_{scat}$  in  $x - z$  plane over which  $\tau_\nu \geq 1$  for Lyman  $\alpha$  cross section  $\sigma_\nu = 10^{-15}$   $\text{cm}^2$ . This cross section corresponds to a velocity  $\simeq 25$  km  $s^{-1}$  from line center.

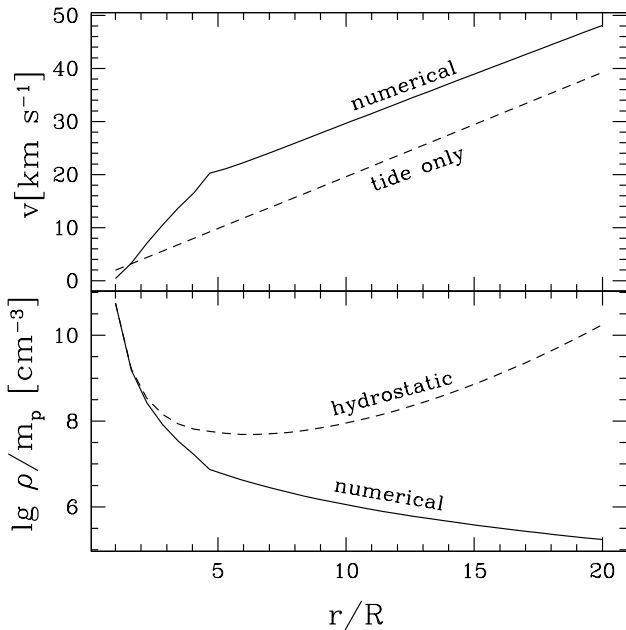


FIG. 11.— Velocity and density versus radius along a field line in the wind zone. Model 1 parameters from Table 1 are used. The field line is located at  $\phi = 0$  with  $\theta_b = 0.35$  rad. The dead zone is at  $\theta_d = 0.48$  rad and the critical field line is at  $\theta_{b,crit} = 0.23$ . The discontinuity at  $r/R = 4.7$  is the dead zone radius, where the field changes shape. The line labeled “tide only” is the asymptotic approximation in eq.39, and the line labeled “hydrostatic” evaluates the density using the hydrostatic balance approximation in eq.19.

way between primary and secondary transit. The quan-

tity plotted is  $\rho/m_p = n_H + n_p$  (note that this quantity is distinct from the total number density  $n_{tot} = n_H + 2n_p$ , which depends on the details of the photoionization model). Model 1 parameters listed in Table 1 were used. Near the planet the contours are approximately spherical, since the velocities are everywhere subsonic and the tidal force is small. The bulge at the equator is the equatorial dead zone. The poles are hydrostatic as tides have shut down the wind, and the inward tidal force at the pole causes the density to decrease outward faster than at the equator. The impact of the tidal force on the dead zone can be seen by comparing the upper and lower panels in Figure 12. Along the  $x$ -direction, the outward tidal force decreases the size of the dead zone, but the same tidal force also causes the dead zone to have higher density. Outside the sonic point, the density in the wind zone is smaller than in the neighboring dead zone, which pushes the density contours inward in the wind zone. Near the equator, outside the dead zone, the density becomes quite small, hence the pile-up of contours near the critical angle  $\sin \theta_{crit}$ .

In the next section, the wind models in Table 1 are used to compute the planetary mass loss rate in the wind zone.

## 10. MASS LOSS RATE AND SPIN-DOWN TORQUE

The mass loss rate is computed by integrating  $\rho v_r = \rho b_r v_b$  over the surface area of the wind zone at the base. Using the base density from eq.18, the mass loss rate is

$$\begin{aligned} \dot{M} &= R^2 \rho_{ss} \int_0^{2\pi} d\phi \int_{\text{wind zone}} d\theta_b \sin \theta_b b_r v_b \left( \frac{\rho_b(\theta_b, \phi)}{\rho_{ss}} \right) \\ &= R^2 P_{ss} a^{-1} \mathcal{F}(\lambda, \epsilon, \beta) \end{aligned}$$

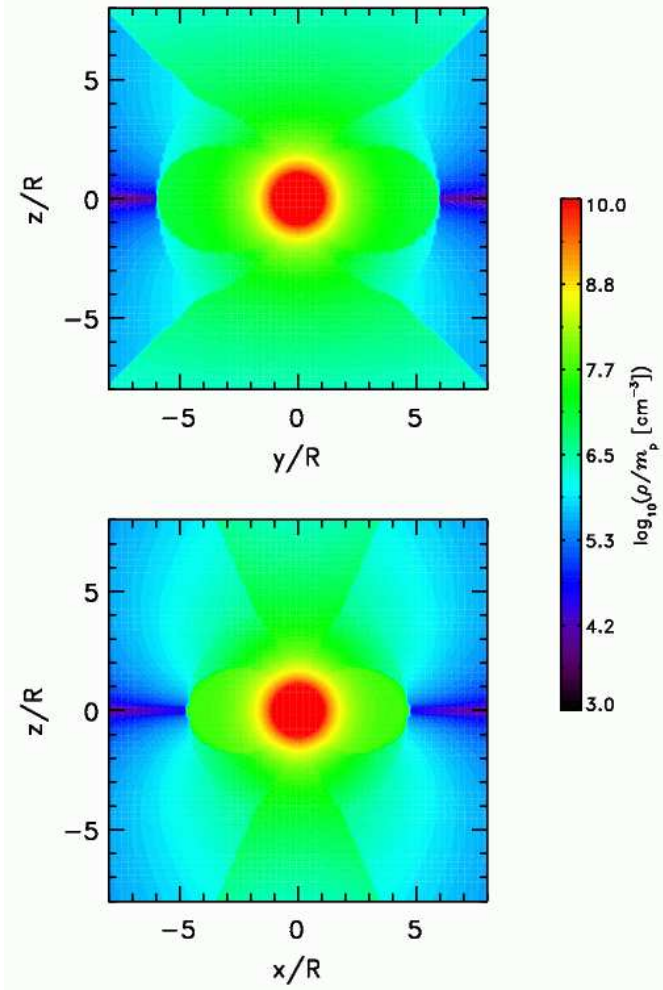


FIG. 12.— Contours of mass density,  $\log_{10} \rho/m_p [\text{cm}^{-3}]$  in the  $y-z$  plane (upper) at  $x=0$ , and in the  $x-z$  plane (lower) for  $y=0$ . Model 1 parameters are used (see Table 1).

$$\begin{aligned}
 &= 4.0 \times 10^{12} \text{ g s}^{-1} \left( \frac{R}{1.4R_J} \right)^2 \\
 &\times \left( \frac{P_{ss}}{0.04 \mu\text{bar}} \right) \left( \frac{10 \text{ km s}^{-1}}{a} \right) \mathcal{F}(\lambda, \epsilon, \beta), \quad (53)
 \end{aligned}$$

where the dimensionless integral

$$\mathcal{F}(\lambda, \epsilon, \beta) = 8 \int_0^{\pi/2} d\phi \int_0^{\theta_d} d\theta_b \sin \theta_b b_r \left( \frac{v_b}{a} \right) \left( \frac{\rho_b(\theta_b, \phi)}{\rho_{ss}} \right) \quad (54)$$

The mass loss rate for fixed  $M$ ,  $R$  and  $B_0$ , but varying  $a$ ,  $D$  and  $P_{ss}$  is shown in Figure 13. The steep decline of  $\dot{M}$  with  $\lambda$  is due to smaller density at the sonic point radius. The mass loss decreases slightly for large  $\epsilon$  due to the smaller fraction of open field lines.

Why is the mass loss rate  $\dot{M}$  proportional to the base pressure  $P_{ss}$ ? Recall that we are approximating the true atmosphere with an isothermal model. The appropriate values of  $a^2$  and  $P_{ss}$ , as determined by photoionization equilibrium and heating/cooling balance, have been discussed in section 8. The sonic point lies at a fixed radius, given roughly by eq.34 based on the choice of sound speed  $a$ . The location of the base of the isothermal layer is also at a fixed radius, estimated to be  $1.1R_{\text{ph}}$  (see § 4). By

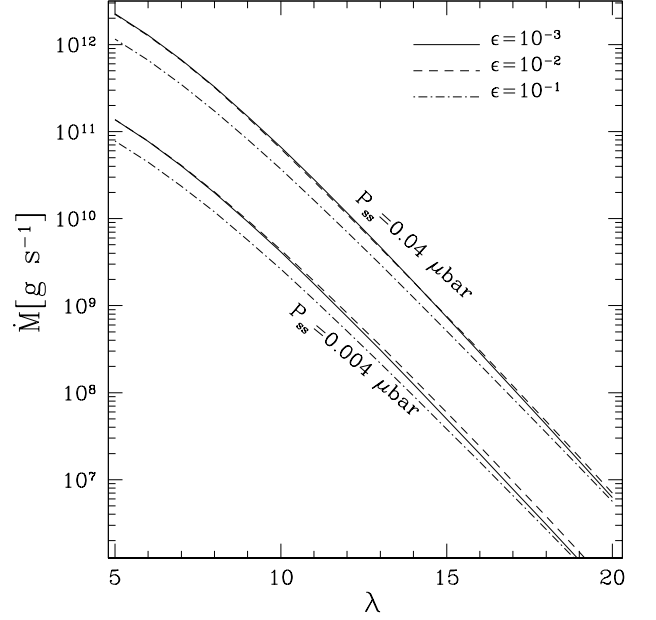


FIG. 13.— Total mass loss rate as a function of  $\lambda$  for  $M_p = 0.7M_J$ ,  $R = 1.4R_J$  and  $B_0 = 8.6 \text{ G}$ . The upper (lower) set of three curves uses base pressure  $P_{ss} = 0.04$  ( $0.004$ )  $\mu\text{bar}$ . The line style in each set of three curves gives the value of  $\epsilon$ , the tidal strength.

eq.19,  $\rho(r=r_s) \propto \rho_{ss}$ , therefore the density at the sonic point is proportional to the base density  $\rho_{ss}$  (and therefore also  $P_{ss}$ ). Consequently, if a larger value of  $P_{ss}$  is required to explain the transit depth, the mass loss must be increased proportionally.

The mass loss rates in Figure 13 are largely consistent with previous studies (e.g., Murray-Clay et al. 2009) when comparable gas density is used. By comparison, an unmagnetized, spherically symmetric, isothermal wind would have (Lamers & Cassinelli 1999)  $\mathcal{F} \simeq \pi \lambda^2 \exp(3/2 - \lambda)$ , which would be a factor of  $\simeq 3 - 10$  larger than the curves in Figure 13, and with a slightly flatter slope. Inclusion of the magnetic field decreases the mass loss rate, mainly due to the decrease in area occupied by the wind zone.

The angular momentum loss rate depends on the radius at which the torque is applied. For an isolated planet, the field lines remain rigid out to the Alfvén radius. But this location may be at many tens of planetary radii, and may be pre-empted by the interaction of the planetary wind with the stellar wind. By assuming the torque is exerted at a radius  $r_{\text{torque}}$  we estimate an angular momentum loss rate

$$\begin{aligned}
 \dot{M} \Omega r_{\text{torque}}^2 &\simeq 7.3 \times 10^{28} \text{ erg} \left( \frac{1 \text{ day}}{P_{\text{orb}}} \right) \\
 &\times \left( \frac{r_{\text{torque}}}{10^{11} \text{ cm}} \right)^2 \left( \frac{\dot{M}}{10^{11} \text{ g s}^{-1}} \right). \quad (55)
 \end{aligned}$$

While this torque may cause moderate changes in the spin rate for an isolated planet on Gyr timescales, it likely not large enough to torque the planet away from synchronous rotation to the extent that significant gravitational tidal heating will occur (see Arras & Socrates 2009, for a discussion of the necessary torques).

## 11. NEUTRAL HYDROGEN COLUMN DENSITY

Given the global MHD models derived in section 9, we require a model for the run of ionization in the magnetosphere in order to compute observable quantities such as the transmission spectrum. In section 8, we discussed a model including only the dominant processes: photoionization and radiative recombination of hydrogen. In the remainder of the paper, we use the simpler optically thin limit to evaluate  $n_H$  given  $\rho$ :

$$n_H = \left( \frac{\sqrt{n_{\text{eq},0} + 4\frac{\rho}{m_p}} - \sqrt{n_{\text{eq},0}}}{2} \right)^2. \quad (56)$$

Here  $n_{\text{eq},0} = J_0/\alpha_B$  is the density at which  $n_H = n_p$  in the optically thin limit. The use of  $J_0$  instead of  $J$  simplifies the calculation, as only the local density is required, and not the column  $N_H$ . This approximation may underestimate  $n_H$  near the H-H<sup>+</sup> transition, but should be adequate for our purposes.

To evaluate the neutral hydrogen column density, we first evaluate  $\rho$  (§ 9), and then  $n_H$  (eq.56), on a grid of  $(x, y, z)$ , with each coordinate in the range  $(-1.1R_*, 1.1R_*)$ . The column is displayed as seen at transit, i.e. we integrate over the coordinate along the star planet line to get column

$$N_H(y, z) = \int_{-1.1R_*}^{1.1R_*} dx n_H(x, y, z) \quad (57)$$

as a function of the impact parameters  $y$  and  $z$ . Figure 14 shows contours of hydrogen column density for the 9 models listed in Table 1. All models have  $M_p = 0.7M_J$  and  $R = 1.4R_J$ , and vary a single parameter  $P_{ss}$ ,  $a$ ,  $B_0$  and  $D$  in turn. The fiducial case, Model 1, clearly shows the equatorial and polar dead zones, as well as the mid-latitude wind zone with comparatively smaller  $N_H$ . Model 2 (3) has  $P_{ss}$  larger (smaller) by a factor of 10. This has the effect of decreasing (increasing) the dead zone size as well as scaling up (down) the density in the dead zone. Model 4 (5) has larger (smaller)  $a$ , leading to larger (smaller) density at a given distance from the planet, as well as increasing (decreasing) the size of the dead zone. Model 6 (7) has larger (smaller)  $B_0$ , which increases (decreases) the size of the dead zone. Model 8 (9) has smaller (larger)  $D$ . Larger tide is more effective in shutting down the wind at the pole, but also decreases the size of the dead zone.

Aside from the overall magnitude mainly set by the base pressure  $P_{ss}$  and sound speed  $a$ , the dominant parameters determining the appearance of each plot are the equatorial and polar dead zone sizes. The equatorial dead zone size (see Figure 5) depends on  $\lambda$ ,  $\beta$  and  $\epsilon$ . The size of the polar dead zone is set by the strength of the tidal force. The critical tidal strength in eq.37 refers to shutting down the wind at  $\theta_b = 0$ , and assumes dipole field geometry. For  $\epsilon > \epsilon_{\text{crit}}$ , a range of  $\theta_b$  near the pole can have the wind shut off. The result depends on the which field geometry is chosen. For instance, the sonic point eq.32 can be rederived for radial field lines. The discriminant of this cubic equation can be used to show that no sonic point can be found for

$$\sin^2 \theta \lesssim \frac{1}{f\epsilon} \left( \epsilon - \frac{32}{27\lambda^2} \right). \quad (58)$$

The critical tidal strength for radial field lines is  $\epsilon_{\text{crit}} = 32/(27\lambda^2)$ , a slightly different numerical coefficient than the dipole case. As  $\epsilon$  increases above  $\epsilon_{\text{crit}}$ , the size of the polar dead zone increases. In the limit  $\epsilon \gg \epsilon_{\text{crit}}$ , the wind is shut down in the entire region  $\sin^2 \theta \leq 1/f$  where the tidal force is inward. For large  $\epsilon$  and small  $\beta$ , the polar and equatorial dead zones can dominate the volume near the planet (e.g., Model 6).

## 12. LYMAN $\alpha$ TRANSMISSION SPECTRA

In section 11 we focused on understanding the hydrogen column as a function of impact parameter, including the dependence on unknown parameters such as temperature and magnetic field. An additional effect on the transmission spectrum is the velocity gradients in the wind, which were studied in sections 7 and 9. In this section we compute the Lyman  $\alpha$  transmission spectra for the global models, including both column and velocity gradient effects.

The transmission function,  $T_\nu$ , is the fraction of stellar flux at frequency  $\nu$  which passes through the planet's atmosphere without suffering scattering out of the beam. In terms of the out-of-transit stellar flux,  $F_\nu^{(0)}$ , and the in-transit flux,  $F_\nu$ ,  $T_\nu$  is defined as

$$T_\nu = \frac{F_\nu}{F_\nu^{(0)}}. \quad (59)$$

If the interstellar medium (ISM) optical depth,  $\tau_\nu^{(\text{ISM})}$ , is constant over the stellar disk, and in time, and the geocoronal emission is independent of time, then the ratio in eq.59 depends solely on the properties of the planetary atmosphere, and is the fundamental quantity to compare to the data.

We compute  $T_\nu$  as follows. Let  $\sigma_\nu$  be the Lyman  $\alpha$  line cross section. We simplify the problem by assuming the planet to be at the center of the stellar disk. The optical depth through the planet's atmosphere at position  $(y, z)$  on the stellar disk is

$$\tau_\nu^{(\text{p})}(y, z) = \int dx n_H(x, y, z) \sigma_\nu(x, y, z). \quad (60)$$

Assuming the stellar intensity is uniform over the disk,

$$T_\nu = \frac{1}{\pi R_*^2} \int dy dz e^{-\tau_\nu^{(\text{p})}(y, z)}, \quad (61)$$

where the integral extends over  $y^2 + z^2 \leq R_*^2$ . As an integrated measure of the transit depth, we compute

$$\frac{\delta F}{F} = \frac{\int d\nu I_\nu^{(*)} e^{-\tau_\nu^{(\text{ISM})}} (1 - T_\nu)}{\int d\nu I_\nu^{(*)} e^{-\tau_\nu^{(\text{ISM})}}} \quad (62)$$

where  $I_\nu^{(*)}$  and  $\tau_\nu^{(\text{ISM})}$  are the unabsorbed stellar intensity and ISM optical depth, both assumed uniform over the disk. In practice, we follow Ben-Jaffel (2008) and integrate over  $-200 \text{ km s}^{-1} \leq \Delta v \leq 200 \text{ km s}^{-1}$ . The interstellar medium (ISM) is assumed to have a temperature  $T_{\text{ism}} = 8000 \text{ K}$  and hydrogen column  $N_{\text{H,ism}} = 10^{18.4} \text{ cm}^{-2}$  (Wood et al. 2005), implying the line is dark inside linewidth  $\Delta v = c(\nu - \nu_0)/\nu_0 \lesssim 50 \text{ km s}^{-1}$ . For  $I_\nu^{(*)}$  we use the following (unnormalized) fit to the quiet solar Lyman  $\alpha$  spectrum



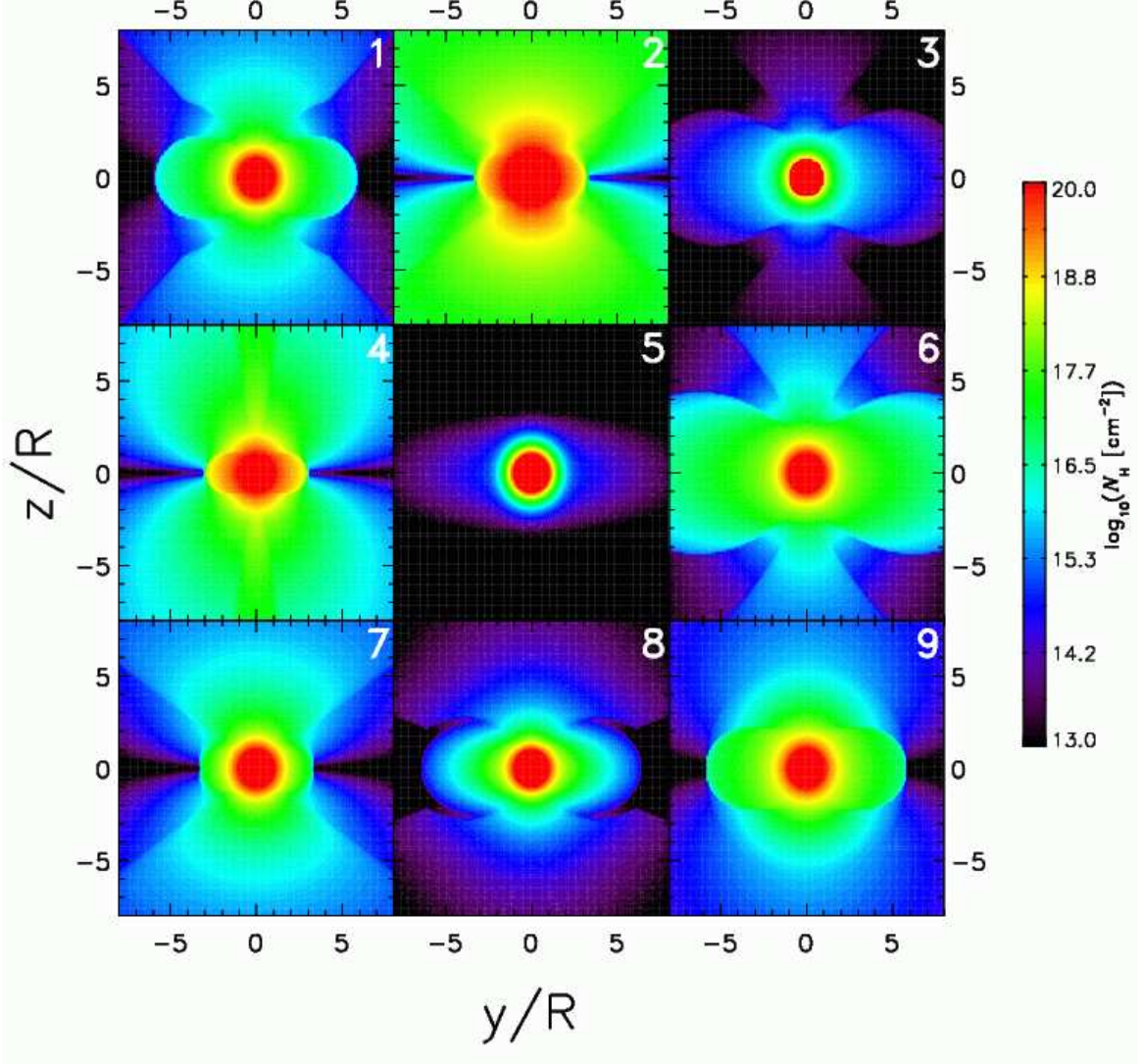


FIG. 14.— Contours of hydrogen column density,  $\log_{10}(N_H[\text{cm}^{-2}])$ , versus impact parameter in the  $y-z$  plane observed during transit. The parameters for each plot are matched to the labeled model numbers in Table 1.

presented in Feldman et al. (1997) (downloaded from <http://www.mps.mpg.de/projects/soho/sumer/FILE/Atlas.html>):

$$I_\nu^{(*)} = \left[ 1 + \left( \frac{\Delta v}{67 \text{ km s}^{-1}} \right)^3 \right]^{-1}. \quad (63)$$

The Voigt function  $H(a, u)$  (Mihalas 1978) is used for the line profile, giving

$$\sigma_\nu = \frac{\pi e^2}{m_e c} f_{12} \frac{1}{\sqrt{\pi} \Delta \nu_D} H(a_D, u) \quad (64)$$

where  $-e$  is the electron charge,  $m_e$  is the electron mass, and  $f_{12} = 0.42$ ,  $\lambda_0 = 1215 \text{ \AA}$  and  $\nu_0 = c/\lambda_0$  are the Lyman  $\alpha$  oscillator strength, line center wavelength and frequency. The Doppler width is  $\Delta \nu_D = \nu_0 v_{\text{th}}/c$  where the hydrogen atom thermal velocity is  $v_{\text{th}} = (2k_b T/m_p)^{1/2}$ . The damping parameter is  $a_D = \Gamma/4\pi\Delta\nu_D$ , where the natural linewidth is  $\Gamma = 6.25 \times 10^8 \text{ s}^{-1}$ . Finally, the distance from line center, in Doppler widths, including both

bulk motion and thermal broadening, is

$$u = \frac{\nu - \nu_0}{\Delta \nu_D} + \frac{v_x}{v_{\text{th}}} \quad (65)$$

where  $v_x$  is the bulk motion directed from planet toward star, which is away from the observer.

There are three instructive limits of eq.61 to guide the intuition. First, if  $v_x = 0$  and the gas is optically thick over an area  $A_{\text{tran}}$ , with negligible optical thickness outside this area, the fraction of flux absorbed by the planet is

$$1 - T_\nu = \frac{A_{\text{tran}}}{\pi R_\star^2} = 0.013 \left( \frac{A_{\text{tran}}}{\pi (1.3 R_J)^2} \right) \left( \frac{1.15 R_\odot}{R_\star} \right)^2 \quad (66)$$

Next, if  $v_x = 0$  and the gas is optically thin, then the transit signal due to the optically thin area is

$$1 - T_\nu \simeq \frac{1}{\pi R_\star^2} \int_{\tau_\nu^{(p)} \ll 1} dy dz \tau_\nu^{(p)}(y, z) \equiv \langle \tau_\nu^{(p)} \rangle, \quad (67)$$

which is just the area-averaged optical depth, and is proportional to the total number of hydrogen atoms times

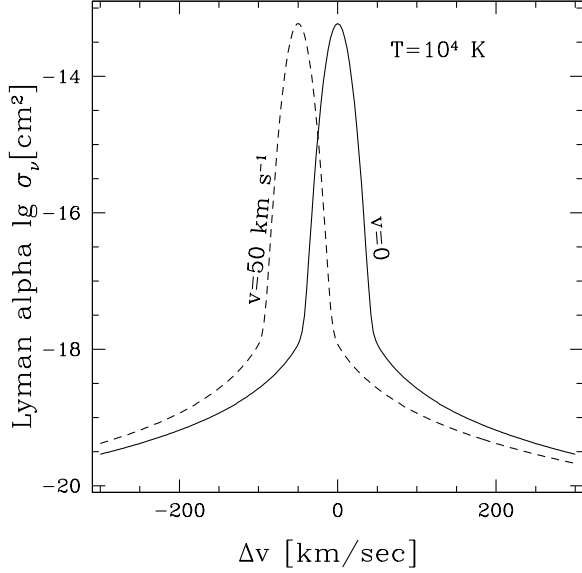


FIG. 15.— Lyman  $\alpha$  cross section as a function of velocity width from line center. Both profiles are given for a temperature  $T = 10^4$  K. The solid line is for zero bulk velocity away from the observer, while the dashed line is for  $\Delta v = 50 \text{ km s}^{-1}$ . For bulk velocity toward the observer, the dashed curve would be reflected about  $\Delta v = 0$ .

their mean cross section. The third limit is when thermal motions are much smaller than bulk motions, and the line profile can be approximated as a delta function  $\delta[\nu - \nu_0(1 - v_x/c)]$ . In this case, the cross section is only nonzero at those values of  $x_* = x_*(\nu, y, z)$  where  $v_x(x_*, y, z) = c(\nu_0 - \nu)/\nu_0$  is satisfied, so that the photon is shifted to line center in the atom's frame. In this case the optical depth becomes

$$\begin{aligned} \tau_\nu^{(p)}(y, z) &= n_H(x_*, y, z) \frac{\pi e^2}{m_e c} f_{12} \frac{\lambda_0}{|\partial v_x(x_*, y, z)/\partial x|} \\ &\simeq 2 \times 10^{-3} \left( \frac{n_H(x_*, y, z)}{1 \text{ cm}^{-3}} \right) \left( \frac{P_{\text{orb}}}{1 \text{ day}} \right) \frac{\Omega}{|\partial v_x(x_*, y, z)/\partial x|} \end{aligned} \quad (68)$$

where in the second equality we have scaled the velocity gradient to the orbital frequency  $\Omega$ . Eq.68 shows that for hydrogen densities  $n_H \gtrsim 10^{2-3} \text{ cm}^{-3}$ , the optical depth along a line of sight will be high provided that there is gas with sufficiently large velocity to absorb at that wavelength.

Figure 15 shows the cross section as a function of frequency in velocity units, at  $T = 10^4$  K and for  $\Delta v = 0$  and  $\Delta v = 50 \text{ km s}^{-1}$ . For HD 209458b, the transit radius is  $R_{\text{ph}} = 1.3R_J$  and the stellar radius is  $R_* = 1.15R_\odot$ , giving a transit depth  $\delta F/F = 0.013$  in the optical continuum. To explain the line-integrated Lyman  $\alpha$  transit depth  $\simeq 9\%$  (e.g., see the discussion in Ben-Jaffel 2008) one could invoke an opaque disk of area  $\sim \pi(2.6R_{\text{ph}})^2$ . The central issue is that this disk must be opaque at  $\Delta v \gtrsim \pm 100 \text{ km s}^{-1}$  from line center, requiring large columns of neutral hydrogen at radii  $2 - 3R_{\text{ph}}$ .

In Figure 10, triangle symbols show where Lyman  $\alpha$  radiation at frequencies  $\pm 100 \text{ km s}^{-1}$  from line center is optically thick on a radial line outward. This point is much deeper in the atmosphere from where Lyman  $\alpha$  continuum at threshold becomes optically thick, due to

the rapid decrease in Lyman  $\alpha$  cross section. Clearly in order to model the transit spectrum in the wavelength region of interest, one must include regions down to  $\sim 1 - 10$  nbar in the atmosphere. To quantify this statement, we compute the optical depth through the H layer where  $n_H \simeq \rho/m_p$  is given by eq.17. Assuming the dominant contribution arises from the layer of steeply falling density, the slant optical depth is dominated by the region near  $x = 0$  and we find

$$\begin{aligned} \tau_\nu^{(p)}(y, z) &= \sigma_\nu \left( \frac{\rho(x=0, y, z)}{m_p} \right) \\ &\times \int dx \exp \left[ -\frac{1}{2a^2} \left( \frac{GM_p}{b^3} - 3\Omega^2 \right) x^2 \right] \\ &\simeq \sigma_\nu \left( \frac{\rho(x=0, y, z)}{m_p} \right) \left( \frac{2\pi b^3/\lambda R}{1 - (b/r_L)^3} \right)^{1/2} \\ &\simeq 1.2 \left( \frac{100 \text{ km s}^{-1}}{\Delta v} \right)^2 \left( \frac{P(x=0, y, z)}{1 \text{ nbar}} \right) \left( \frac{10 \text{ km s}^{-1}}{a} \right)^2 \\ &\times \left( \frac{10}{\lambda} \right)^{1/2} \left( \frac{b}{R} \right)^{3/2} \left( \frac{R}{1.3 R_J} \right) (1 - (b/r_L)^3)^{-1/2}. \end{aligned} \quad (69)$$

Here  $b = \sqrt{y^2 + z^2}$  is the impact parameter, eq.3 was used for the tidal potential,  $r_L$  is given by eq.7, and the last equality assumes the cross section is on the damping wing (see Figure 15). In the  $H^+$  layer, eq.69 should be multiplied by  $1/2$  to account for the smaller H atom scale height. Eq.69 agrees roughly with the position of the triangles in Figure 10, keeping in mind that the slant length is a factor of a few larger than the scale height. Eq.69 shows that the Lyman  $\alpha$  transmission spectrum at  $\Delta v = \pm 100 \text{ km s}^{-1}$  is probing down to  $\lesssim$  nbar pressures, depending on the value of  $b/R$ .

To give a more precise numerical estimate of the transit depth, we first compute the integrated quantity  $\delta F/F$  as in eq.62 for the 9 models in Table 1. The result is given in the table. The velocity range is taken to be  $-200 \leq \Delta v[\text{km s}^{-1}] \leq 200$ . Since  $1 - T_\nu$  decreases away from line center,  $(1 - T_\nu)F_\nu^{(0)}$  is peaked somewhat closer to line center than  $F_\nu^{(0)}$ , the amount depending on the details of the atmosphere. Transit depths of the correct magnitude  $\delta F/F \sim 5 - 10\%$  can be achieved by adjusting the main parameters,  $P_{\text{ss}} \simeq 10 - 100$  nbar and  $a \simeq 8 - 12 \text{ km s}^{-1}$  to have values as expected from the 1D model in Figure 10. The parameters  $B_0$  and  $D$  have a lesser impact by comparison.

The frequency dependent transit depth,  $1 - T_\nu$ , was computed as in eq.61 for the 9 models listed in Table 1, and compared to the data for  $(F_\nu^{(0)} - F_\nu)/F_\nu^{(0)}$  from Figure 6 of Ben-Jaffel (2008). The results are shown in Figure 16. Near line center, nearly the entire planetary atmosphere is optically thick, and absorption is nearly complete. Moving out from line center in the Doppler core, the cross section eventually becomes small enough that part of the atmosphere becomes optically thin, after which  $1 - T_\nu$  decreases rapidly. The curves level out when the damping wing is reached, after which  $1 - T_\nu$  decreases slowly as the  $\tau_\nu^{(p)} = 1$  point moves deeper into the atmosphere as  $P(x=0, y, z) \propto \Delta v^2$ .

Given the large error bars, a range of parameter space

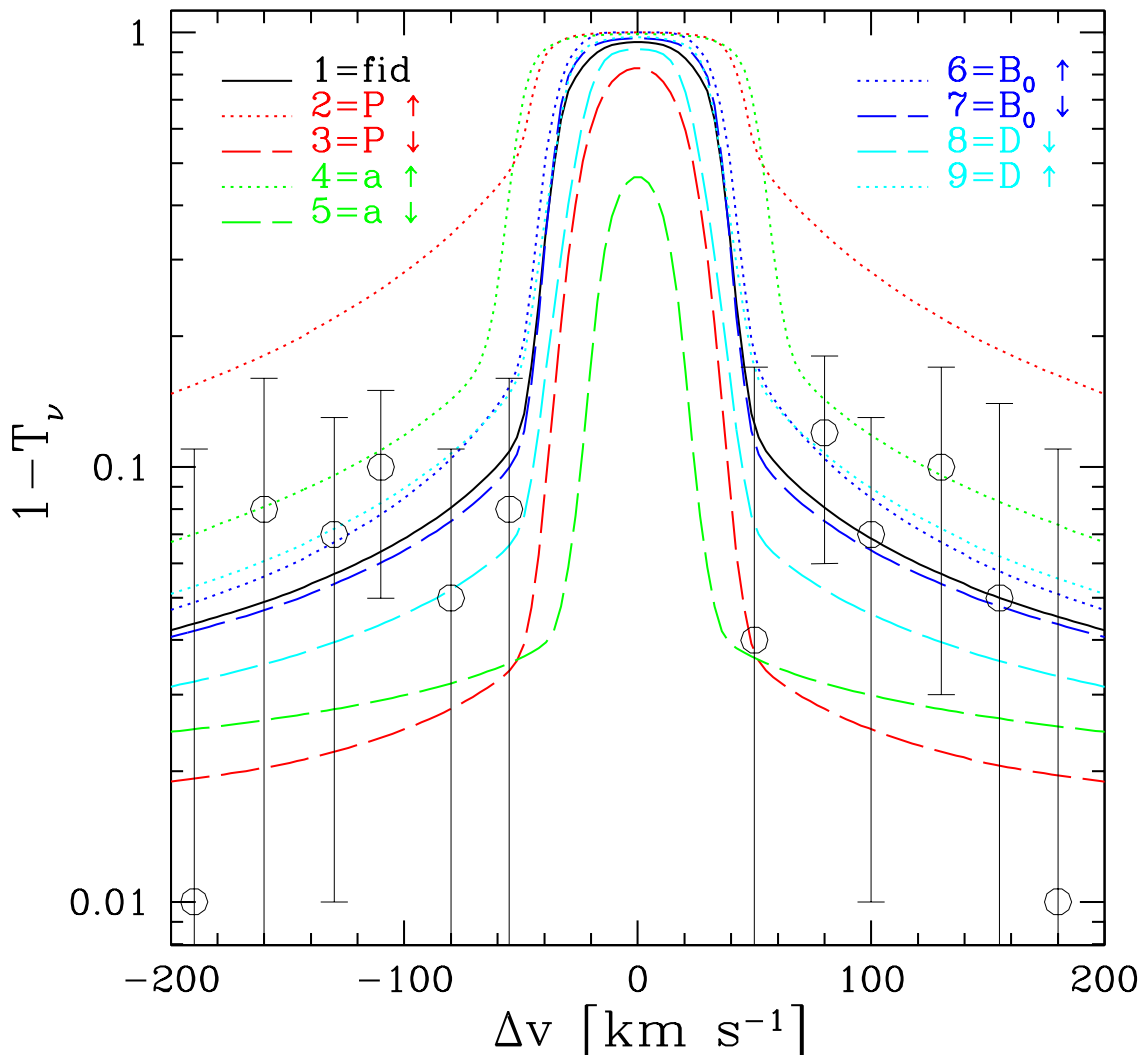


FIG. 16.— Fractional flux decrease,  $1 - T_\nu$ , versus frequency in velocity units for HD 209458b. Curves for Models 1-9 from Table 1 are computed from eq.61 and points with error bars are the data from Figure 6 of Ben-Jaffel (2008).

agrees with the data *if* the warm H layer extends sufficiently deep. For instance, Model 3 with base pressure  $P_{ss} = 4$  nbar is well below the data points with the smallest error bars, in agreement with Murray-Clay et al. (2009). The most sensitive parameter dependencies are with the base pressure,  $P_{ss}$ , and the sound speed (temperature),  $a$ . Increasing the magnetic field has the effect of increasing  $1 - T_\nu$  due to larger  $N_H$  in the magnetosphere. Somewhat offsetting this effect is that increasing  $B_0$  decreases the size of the wind zone, which decreases absorption near line center due to velocity gradients. Perhaps counter-intuitively, moving the planet further from the star increases the transit depth. Inspection of Figure 10 shows that the H extends to both lower pressure and larger radius for more distant planets with atmospheres in photoionization equilibrium. Lastly, we note that velocity gradients are only important for  $\Delta v \lesssim 50$  km s $^{-1}$ , and are more important for smaller  $D$  due to the larger tidal force.

We end this section with a brief discussion of scatter-

ing of Lyman  $\alpha$  from H atoms in the magnetosphere. The problem with observing Lyman  $\alpha$  during transit is that large  $N_H$  is required to create  $\tau_\nu^{(p)} \simeq 1$  at  $\Delta v \gtrsim 100$  km s $^{-1}$ . By contrast, at line center the cross section is  $\sim 10^5$  times larger, implying the atmosphere is optically thick at line center out to much larger radii. We suggest that scattering of stellar Lyman  $\alpha$  during the orbital phases in which the planet is moving toward or away from the observer may be detectable, and provides a probe of thermal gas in the magnetosphere, complementary to the transmission spectrum measured during transit. During the orbit, the Doppler shift of the scattered spectrum varies in time due to the variation in line-of-sight orbital motion. The orbital velocities naturally produces a feature in the spectrum well outside the line core where ISM absorption dominates.

For a planet in circular orbit, there is no relative radial motion with respect to the star, and the stellar spectrum at the planet is not Doppler shifted. However, when an

H atom in the planet resonantly scatters a stellar photon, that H atom is moving with respect to the observer due to the planet’s orbital motion. Photons emitted by the star near line center ( $\Delta v \lesssim 67 \text{ km s}^{-1}$ ) have their frequencies shifted by  $v_{\text{orb}} = 210 \text{ km s}^{-1} (1 \text{ day}/P_{\text{orb}})^{1/3}$  (for a solar mass star) due to the planet’s orbital motion. To assess the area presented by the magnetosphere, we computed the area in the  $x - z$  plane for which  $\tau_{\nu}^{(p)} \gtrsim 1$  for  $\sigma_{\nu} = 10^{-15} \text{ cm}^2$ , which corresponds to  $\Delta v = 25 \text{ km s}^{-1}$  from line center for  $T = 10^4 \text{ K}$ . The results are tabulated in Table 1. We find that the effective radius of the scattering disk is  $r_{\text{sc}} \sim (5 - 10)R$  for the models shown. The scattering disk for Lyman  $\alpha$  is significantly larger than the radius inferred during transit. Assuming none of the resonantly scattered Lyman  $\alpha$  photons are absorbed, and also assuming the Lambert phase function (Hapke 1993) as an estimate, the reflected flux is  $F_{\text{refl}}(\nu) = F_{\star}(\nu')(2/3\pi)(r_{\text{sc}}/D)^2$ , where  $\nu \simeq \nu_0 \pm v_{\text{orb}}$  is the observed frequency,  $\nu' \simeq \nu_0$  was the frequency emitted by the star before Doppler shift, and  $F_{\star}(\nu)$  is the stellar Lyman  $\alpha$  spectrum. The size of the reflected flux relative to the flux emitted by the star out on the wing at frequency  $\nu$  is then  $F_{\text{refl}}(\nu)/F_{\star}(\nu) = (F_{\star}(\nu')/F_{\star}(\nu))(2/3\pi)(r_{\text{sc}}/D)^2$ . Inspection of eq.63 shows that the line center flux is  $\simeq 30(\Delta v/200 \text{ km s}^{-1})^3$  times larger than that at  $\Delta v$ . This acts to enhance the scattered flux signal relative to the background flux level. Numerically we find the ratio of scattered, Doppler shifted flux to background stellar flux is then  $F_{\text{refl}}(\nu)/F_{\star}(\nu) \simeq 0.4(r_{\text{sc}}/10R_J)^2(1 \text{ day}/P_{\text{orb}})^{7/3}$ . While this signal may be small for HD 209458b at  $P_{\text{orb}} = 3.5$  days,  $F_{\text{refl}}(\nu)/F_{\star}(\nu) \simeq 0.02(r_{\text{sc}}/10R_J)^2$ , for planets with  $P_{\text{orb}} = 1 - 2$  days it may be large enough to be observable.

### 13. COMPARISON TO ROCHE-LOBE OVERFLOW

The magnetic wind model developed in this paper differs in several respects from purely hydrodynamic mass loss models (e.g., Lubow & Shu 1975). In the standard Roche-lobe model for nearly equal mass stars, nearly all the gas leaves the donor in a narrow, cold stream through the L1 Lagrange point. The first assumption underlying this solution is that  $r_{s,0} \gg r_{L1}$ , so that the gas is subsonic at the L1 equipotential for most  $(\theta, \phi)$ . From eq.7 and eq.34, this ratio is  $r_{s,0}/r_L = (\epsilon\lambda^2/9)^{1/3}$ , and hydrodynamic Roche lobe overflow requires  $\epsilon \gg 9/\lambda^2$ . Figure 6 plots  $\epsilon$  versus  $\lambda$ , and shows that most, but not all, transiting planets are indeed in the  $r_{s,0} \gg r_L$  regime; ignoring magnetic effects, Roche lobe overflow would then be a good approximation. In the opposite limit of  $\epsilon \ll 9/\lambda^2$ , the solution would more closely resemble a thermally driven wind weakly perturbed by tides. The second assumption underlying a narrow flow through L1 is that the mass ratio of the two bodies is near unity. Although the tidal expansion  $r \ll D$  in eq.3 ignores the difference in potential between the L1 and L2 Lagrange points, inclusion of higher order terms gives  $U_{L2} - U_{L1} \simeq 2GM_p/(3D)$  for the potential difference (Murray & Dermott 2000). When the ratio  $2GM_p/(3Da^2) = (2/3)(\epsilon\lambda M_p/M_{\star})^{1/3} \ll 1$ , the density difference between the L1 and L2 points is small, and nearly equal mass loss is expected through L1 and L2. While mass loss through L1 enters into an orbit around the star, mass loss through L2 leads to gas in a circumbi-

nary orbit.

MHD effects, in particular the existence of a dead zone, further limit the applicability of the Roche lobe model. If the planet has a sufficiently large magnetic field that the L1 Lagrange point lies inside the dead zone, gas pressure is insufficient to open the magnetic field lines and the flow through the L1 point is expected to be choked off. Also, the magnetic field may torque the gas, keeping it in corotation with the planet out to the Alfvén radius. By contrast, if  $B^2/8\pi \ll P \simeq \rho v^2$  at the sonic point, and  $r_{s,0} \gg r_L$ , magnetic stresses and tides may be ignored the Roche-lobe model is expected to be recovered.

For the models of HD 209458b considered in this paper, inspection of Table 1 shows that  $r_{s,0}$ ,  $r_L$  and the dead zone radius  $r_d$  may be within factors of a few of each other, and the situation is more complex than the simplified Roche-lobe overflow model permits.

### 14. SUMMARY AND DISCUSSION

The objective of this paper was to develop a model for the upper atmospheres of hot Jupiters, including the influence of a dynamically important magnetic field. Our starting point (§’s 2, 3, 4, 6, 7, 9 and Appendix A) was to estimate field strengths for hot Jupiters, and to apply the theoretical model developed for MHD winds from stars to the case of winds escaping from the upper atmospheres of planets. In the process, we included strong tidal forces from the parent star (§’s 5, 6, and 7). We computed a 1D model of the temperature profile and ionization state of the atmosphere (§ 8), and constructed maps of neutral hydrogen column and fluid velocities to understand the mass loss and transmission spectra of HD 209458b (§’s 9, 10, 11, and 12). We contrast this model to the standard Roche-lobe overflow model (§ 13) and verify, *a posteriori*, the validity of the MHD approximation (Appendix B).

In section 3, we discussed the application of dynamo models to understand the magnetic field strength generated by the planet, which is currently unconstrained by observations. Using the recent results of Christensen et al. (2009), which showed that the dynamo field increases with heat flux in the planet’s core, we argued that the large radii of hot Jupiters, and hence large core flux, imply that the magnetic fields of inflated hot Jupiters may be larger than Jupiter’s field. This motivated exploring a wide range of possible magnetic field strengths, both smaller and larger than Jupiter’s field.

The formation of a dead zone, in which gas pressure is insufficient to open up magnetic field lines, was motivated with a toy problem (§ 2) as intuition for understanding the detailed structure of the hydrostatic model (§ 6). The projection of the tidal force along magnetic field lines was used to derive the “magnetic Roche lobe radius” (§ 5), outside of which gravity points outward along the magnetic loop. Net gravity can point outward for loops slightly larger than the distance to the L1-L2 Lagrange points, even in the plane perpendicular to the star-planet line. As a result of net outward gravity, the density may increase outward, as shown in Figure 4. We defined the key parameters  $\lambda$  and  $\epsilon$ , characterizing the binding energy of the gas and the strength of tides, and their values for the observed transiting planets were given in Figures 2 and 3. Many close-in planets have weakly bound atmospheres with  $\lambda \lesssim 10$ , and are subject to strong tidal forces with  $\epsilon \gtrsim 0.1$ . The magnetic field

strength was characterized by the plasma  $\beta$  evaluated at the base of the atmosphere. Solutions for the radius of the dead zone depend on the parameters  $\lambda$ ,  $\beta$  and  $\epsilon$ , as shown in Figure 5. We found that for typical parameters, the dead zone extends to  $\simeq (3 - 20)R$ , implying that much of the volume of the magnetosphere near the planet is occupied by bound gas with no bulk velocity. Even gas outside the Roche-lobe radius can be static, if the dead zone is larger than the Roche-lobe radius.

Open field lines, which are capable of supporting an outflow, were discussed in section 7. The momentum equation along field lines was used to compute the positions of the (slow magneto)sonic points for a set of models using dipole geometry. Analytic solutions in the limit of strong and weak tides were given, which illustrated that inward tidal forces at the magnetic poles (for a magnetic dipole moment aligned with the orbital angular momentum axis) may eliminate the sonic point solutions near the planet. Thus, sufficiently strong tides effectively shut off the wind, creating a second dead zone at the poles. Figures 7 and 8 show solutions for sonic point radius and base velocity versus footpoint position. When the sonic point position moves far from the planet, the base velocity becomes small, and the field lines are effectively hydrostatic. Depending on  $\epsilon$  and  $\beta$ , the equatorial and polar dead zones may dominate the volume near the planet. Lastly, we estimated the asymptotic flow speed due to tides in eq.40, showing that  $v_{\text{asympt}} \ll 100 \text{ km s}^{-1}$  for the orbital periods and stellar radii of interest. Consequently, bulk motion cannot affect the Lyman  $\alpha$  line profile at  $\Delta v \gtrsim 100 \text{ km s}^{-1}$  from line center.

As a prelude to discussion of global models of the magnetosphere, and the Lyman  $\alpha$  transmission spectrum, we presented a simple spherical model of photoionization and thermal balance (§ 8) in order to assess the size of the “warm” neutral H layer. We computed the depth dependence of photoelectric heating in Figure 9, showing that the heating drops off with pressure as a power-law, rather than an exponential, into the atmosphere. The resulting photoelectric heating, which we assumed was balanced by collisionally-excited Lyman  $\alpha$  cooling, gives temperatures  $T \simeq (5 - 10) \times 10^3 \text{ K}$  down to pressures  $P \simeq (10 - 100) \text{ nbar}$ . As a result, this neutral H layer contributes significantly to the radius, as shown in Figure 10. As first stressed by Koskinen et al. (2010), the location of the warm H layer is key in understanding the large observed transit depths  $\delta F/F \sim 5 - 10\%$ . The transit depth due to the layer extending upward from the H-H<sup>+</sup> ionization layer alone is too small to explain the observations of HD 209458b, as discussed in detail by Murray-Clay et al. (2009).

Global models of the magnetosphere were constructed (§ 9), both to compute mass loss rates (§ 10), and to construct maps of the neutral hydrogen column densities for a range of parameters as observed during transit (§ 11). A by-product of the warm, deep H layer is a larger mass loss rate than in studies with more shallow H layers (e.g., Murray-Clay et al. 2009). The net mass loss rates are still insufficient to evaporate the planet, and are reduced by a factor of 3-10 due to the presence of the magnetic field for the parameters used. The largest columns within a few  $R$  of the planet occur in the dead zones, and may receive a contribution from H atoms outside the Roche lobe, but which are still bound to the planet. Hence,

the observation of H atoms outside the Roche lobe alone cannot be stated as evidence for mass loss.

The 9 global models in Table 1 were used to compute Lyman  $\alpha$  transmission spectra in section 12. We stress that the observational quantity most directly comparable with models of the magnetosphere is the fractional flux decrease between in and out of transit spectra — this quantity is relatively independent of ISM absorption, geocoronal contamination, and the background stellar spectrum, and is directly computable from atmosphere models. The comparison between the models and data for HD 209458b from Ben-Jaffel (2008) is shown in Figure 16. By variation of the base pressure of the warm H layer, and temperature, models can be made to bracket the data points, although the large error bars do not allow precise determination of the atmosphere’s parameters. Increased magnetic field is shown to increase the transit depth, as does moving the planet further from the star.

A comparison of the MHD wind model presented in this paper with the more commonly-used Roche-lobe overflow model was given in section 13. It was argued that different regimes of accretion are possible depending on the position of the sonic point (of an isolated body), the L1-L2 Lagrange points, and the size of the dead zone. In particular, if the L1 Lagrange point is inside the dead zone, gas pressure is insufficient to open up the magnetic field lines, and a narrow flow through L1 is not possible. These considerations suggest that mass loss from hot Jupiters may be more complex than the simple Roche-lobe overflow model. Estimates of collision rates in the atmosphere (Appendix B) demonstrate the validity of the MHD approximation, that the e-p-H gas is well-coupled collisionally at the expected densities and temperatures in the atmosphere, and that even neutral H gas cannot ballistically escape the planet.

The model presented in this paper shows that magnetic fields may strongly affect theoretical estimates of fluid density and velocity in the upper atmosphere, and even the interpretation of transit depths, since neutral H atoms outside the Roche-lobe radius may not be escaping. In future work, we hope to include additional physical effects, such as the interaction with the stellar wind, more detailed photoionization calculations including heavy elements, and collisional (non-MHD) effects, which will allow a more comprehensive physical picture of the upper atmospheres of hot Jupiters.

We thank many colleagues for discussions, including Sean Matt on MHD wind theory, Chris Matzner on photoionization equilibrium in dipole geometry, Jean Michel Desert and David Sing on observations, Craig Sarazin on cooling physics, Lars Bildsten on CV systems, and Anne Verbitser on the Lyman  $\alpha$  scattering. We also thank the referee for feedback that improved the paper. GT gratefully acknowledges support from NASA’s sponsorship of the Virginia Space Grant Consortium and a Teaching & Technology Support Partner Fellowship from the University of Virginia. PA thanks the Kavli Institute for Theoretical Physics and participants in the program “Theory and Observation of Exoplanets” for a stimulating visit. This work was supported in part by NSF (AST-0908079) and NASA Origins (NNX10AH29G) grants. PA is an

Alfred P. Sloan Fellow, and gratefully acknowledges support from the University of Virginia's Fund for Excellence in Science and Technology.

## APPENDIX

### A. MHD WIND EQUATIONS

In this appendix, we present the MHD equations and discuss how currents produced in the magnetosphere modify the field produced by the planet's core. This discussion motivates our choice of field geometry used in the global models.

There is a well developed literature for axisymmetric winds from rotating, magnetized stars. An excellent review is given by Spruit (1996). Here we rely heavily on the analytic studies in Mestel (1968) and Mestel & Spruit (1987). The inclusion of the magnetic field can greatly affect the mass loss rate and wind speed for sufficiently fast rotation. We are not aware of detailed studies of wind launching from rotating magnetized bodies including the non-axisymmetric tidal acceleration. We postpone a numerical study of such a problem to a future investigation, here using a semi-analytic treatment.

The three-dimensional MHD equations for steady isothermal flow in the frame corotating with the planet are mass continuity

$$\nabla \cdot (\rho \mathbf{v}) = 0, \quad (\text{A1})$$

the Euler equation

$$\mathbf{v} \cdot \nabla \mathbf{v} + 2\boldsymbol{\Omega} \times \mathbf{v} = -a^2 \nabla \ln \rho - \nabla U + \frac{\mathbf{J} \times \mathbf{B}}{c\rho}, \quad (\text{A2})$$

Ohm's law for infinite conductivity

$$\mathbf{E} = -\mathbf{v} \times \mathbf{B}/c, \quad (\text{A3})$$

the induction equation

$$\nabla \times \mathbf{E} = -\frac{1}{c} \nabla \times (\mathbf{v} \times \mathbf{B}) = 0, \quad (\text{A4})$$

Ampere's equation

$$\nabla \times \mathbf{B} = \frac{4\pi}{c} \mathbf{J}, \quad (\text{A5})$$

the isothermal equation of state

$$P = \rho a^2, \quad (\text{A6})$$

and the no monopoles condition

$$\nabla \cdot \mathbf{B} = 0. \quad (\text{A7})$$

We have used constant  $a^2$  to rewrite the pressure gradient as  $-\nabla p/\rho = -a^2 \nabla \ln \rho$ . The isothermal approximation is justified in section 8. The Coriolis and centrifugal forces appear in eq.A2 as we work in a corotating frame (see section 5).

To gain further insight, we rewrite eq.A2 using the vector identity  $\mathbf{v} \cdot \nabla \mathbf{v} = \nabla(v^2/2) - \mathbf{v} \times (\nabla \times \mathbf{v})$  to obtain

$$\nabla W = \mathbf{v} \times (2\boldsymbol{\Omega} + \nabla \times \mathbf{v}) + \frac{1}{\rho c} \mathbf{J} \times \mathbf{B} \quad (\text{A8})$$

where

$$W \equiv \frac{1}{2}v^2 + a^2 \ln \rho + U. \quad (\text{A9})$$

Constants of the motion can be derived by dotting eq.A8 with  $\mathbf{B}$  to eliminate the Lorentz force. We find

$$\mathbf{B} \cdot \nabla W = - (2\boldsymbol{\Omega} + \nabla \times \mathbf{v}) \cdot (\mathbf{v} \times \mathbf{B}) = 0, \quad (\text{A10})$$

since the electric field vanishes in the co-rotating frame (Spruit 1996). Hence  $W$ , the Bernoulli constant, is constant along field lines. Another way to understand the work done on the gas is to dot eq.A8 with  $\mathbf{v}$ :

$$\rho \mathbf{v} \cdot \nabla W = \nabla \cdot (\rho \mathbf{v} W) = -\frac{1}{c} \mathbf{v} \cdot (\mathbf{B} \times \mathbf{J}) = \mathbf{J} \cdot \mathbf{E} = 0. \quad (\text{A11})$$

In the rotating frame, work is done on the gas by  $-\nabla U$ , while in the inertial frame the electromagnetic field performs  $\mathbf{J} \cdot \mathbf{E}$  work on the gas (Spruit 1996).

To understand the magnetic field structure in more detail, we take the cross product of eq.A8 with  $\mathbf{B}$  to obtain the equation of trans-field force balance. Solving this equation for the component of current perpendicular to  $\mathbf{B}$  we find

$$\frac{4\pi}{c} \mathbf{J}_\perp \equiv \frac{4\pi}{c} (\mathbf{J} - \mathbf{b}\mathbf{b} \cdot \mathbf{J}) = \frac{1}{v_A^2} \mathbf{B} \times [\nabla W + (2\boldsymbol{\Omega} + \nabla \times \mathbf{v}) \times \mathbf{v}]. \quad (\text{A12})$$

Here  $v_A = B/\sqrt{4\pi\rho}$  is the Alfvén speed. This equation describes the perpendicular currents that must flow in order to achieve perpendicular force balance. In axisymmetry, this equation is often called the modified Grad-Shafranov equation (Heinemann & Olbert 1978; Lovelace et al. 1986). Perpendicular currents arise due to either vorticity in the flow, or variation of the Bernoulli constant from one field line to the next. In the dead zone, the fact that  $\mathbf{v} = 0$ , and the further assumption that  $W$  is constant at the base, implies that  $\mathbf{J}_\perp = 0$  in the dead zone. Parallel currents are determined from  $\mathbf{J}_\perp$  by charge conservation,  $\nabla \cdot \mathbf{J} = 0$ .

An order of magnitude estimate for the fields  $\delta\mathbf{B}$  created by volume currents  $\mathbf{J}_\perp$ , compared to the planetary dynamo-generated fields  $\mathbf{B}_p$  is

$$\frac{B_\perp}{B_p} \sim \frac{r}{B} \frac{4\pi}{c} J_\perp \sim \frac{\max(a^2, v^2, \Omega r v, (\Omega r)^2)}{v_{A,p}^2}, \quad (\text{A13})$$

where  $v_{A,p} = B_p/\sqrt{4\pi\rho}$ . The terms separated by commas on the right hand side of eq.A13 are estimates of the individual terms in eq.A12. This estimate shows that volume currents can only significantly perturb the field out near the Alfvén radius where  $v \sim \Omega r \sim v_{A,p}$ . As we now discuss, at much smaller radii, of order the dead zone radius, the field is already strongly perturbed by current sheets.

Mestel (1968) and Mestel & Spruit (1987) discussed the matching conditions between the dead and wind zones. The finite velocity in the wind zone acts to decrease the pressure there relative to the dead zone. Integrating the momentum equation across the dead zone-wind zone boundary, the total gas plus magnetic pressure must be continuous, so that the magnetic field strength must increase moving from the dead to the wind zone. This implies the existence of a current sheet separating the dead and wind zone boundaries, as shown in Figure 1. Letting the subscripts “d” and “w” denote quantities just inside the dead and wind zones, respectively, total pressure continuity can be written

$$P_d + \frac{B_d^2}{8\pi} = P_w + \frac{B_w^2}{8\pi}. \quad (\text{A14})$$

For identical conditions at the base, the Bernoulli equation relates the pressures as  $P_w \simeq P_d \exp(-v^2/2a^2)$ . Considering only the dipole field from the planet,  $B_p$ , and the field  $\delta B \simeq 2\pi K/c$  produced by current per unit length,  $K$ , the fields in the dead and wind zones are  $B_w = B_p + \delta B$  and  $B_d = B_p - \delta B$ . Plugging in to eq.A14 the solution for the line density is

$$\frac{K}{c} = \frac{P_d}{B_p} \left(1 - e^{-v^2/2a^2}\right). \quad (\text{A15})$$

The ratio of the field produced by the sheet current compared to that from the planet’s core is then

$$\frac{\delta B}{B_p} \simeq \frac{1}{4} \beta_d \left(1 - e^{-v^2/2a^2}\right) \quad (\text{A16})$$

where  $\beta_d = 8\pi P_d/B_p^2$  is the beta for the planetary field just inside the dead zone. Inside the sonic point in the wind zone,  $v \ll a$  and sheet currents only slightly perturb the field since  $\delta B/B \sim \beta_d v^2/8a^2 \sim (v/2v_A)^2 \ll 1$ . Outside the sonic point, where  $v/a \gg 1$ , we find  $\delta B/B_p \sim \beta_d/4$ , which increases outward. Hence the field configuration is expected to be significantly altered from the dipole outside the  $\beta_d \sim 1$  point in the wind zone. As we have assumed that  $\beta \gg 1$  at the sonic point, we expect the field to be altered in between the sonic and Alfvén points.

In addition to the sheet currents at the dead zone-wind zone boundary, there is a sheet current at the equator in the wind zone. This sheet current causes the reversal in sign of the field near the equator, approaching the split monopole form  $\mathbf{B} \propto r^{-2} \mathbf{e}_r$  sufficiently distant from other current sources near the planet. Since  $K \propto B_r \propto 1/r^2$  in the wind zone, and  $K \propto \beta_d$  increases in the dead zone, we expect the maximum current to occur near the cusp in the magnetic field. The polar dead zone is expected to have a smooth transition from dead to wind zone, as Figure 8 shows a gradual transition. We expect volume currents in this transition, rather than true sheet currents.

Based on these analytic estimates, an approximate field geometry in the wind zone is roughly dipolar inside the dead zone radius and roughly straight field lines outside. To go beyond this would require a detailed solution of the trans-field force balance for the field geometry, which is beyond the scope of the present work.

## B. MEAN FREE PATHS, ION-NEUTRAL DRIFT AND OHM’S LAW

In this section we discuss the relative motion of the e-p-H gas as well as the magnetic field for the conditions relevant to hot Jupiters (see Figure 10). Equations and collision rates are taken from Schunk & Nagy (2004), SN hereafter.

To simplify the calculation, we assume all three species are isothermal with temperature  $T$ , and we work in the “diffusion approximation” in which inertial terms are ignored in the fluid equations of each species. Let  $\mathbf{v}_j$  be the mean velocity of species  $j$ ,  $\mathbf{E}$  the electric field, and  $\nu_{jk}$  the momentum-transfer collision rate between species  $j$  and

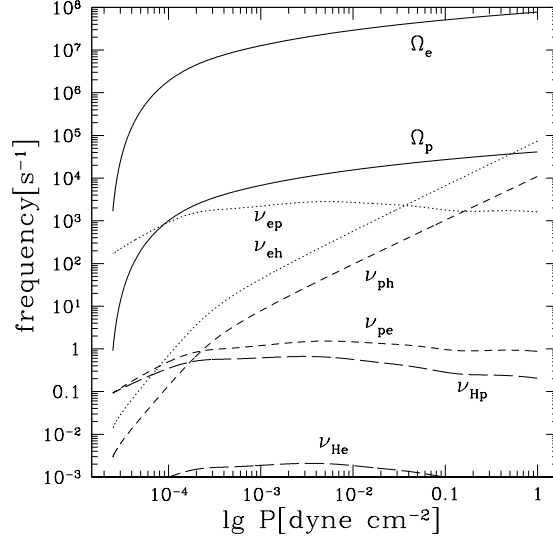


FIG. 17.— Gyration and collision frequencies versus depth for the model shown in Figure 10.

TABLE 2  
COLLISION AND GYRATION FREQUENCIES

$\Omega_e = \frac{eB}{m_e c} = 1.8 \times 10^7 \text{ rad s}^{-1} \text{ (B/1G)}$	electron cyclotron	
$\Omega_i = \frac{eB}{m_p c} = 9.6 \times 10^3 \text{ rad s}^{-1} \text{ (B/1G)}$	proton cyclotron	
$\nu_{eH} = 6.4 \text{ s}^{-1} (n_H/10^8 \text{ cm}^{-3})$	polarization	SN eq.4.88 and table 4.1
$\nu_{He} = 3.5 \times 10^{-3} \text{ s}^{-1} (n_e/10^8 \text{ cm}^{-3})$	polarization	SN eq.4.88 and table 4.1
$\nu_{ep} = 3700.0 \text{ s}^{-1} (n_p/10^8 \text{ cm}^{-3}) (10^4 \text{ K/T})^{3/2} (\ln \Lambda_{ep}/10)$	Coulomb	SN eq.4.140, 4.56
$\nu_{pe} = 2.0 \text{ s}^{-1} (n_e/10^8 \text{ cm}^{-3}) (10^4 \text{ K/T})^{3/2} (\ln \Lambda_{pe}/10)$	Coulomb	SN eq.4.140, 4.56
$\nu_{pH} = 1.2 \text{ s}^{-1} (n_H/10^8 \text{ cm}^{-3}) (T/10^4 \text{ K})^{1/2}$	Charge exchange	SN table 4.5
$\nu_{Hp} = 1.2 \text{ s}^{-1} (n_p/10^8 \text{ cm}^{-3}) (T/10^4 \text{ K})^{1/2}$	Charge exchange	SN table 4.5

$k$ . Momentum conservation implies  $n_j m_j \nu_{jk} = n_k m_k \nu_{kj}$ . We follow Braginskii (1965) and ignore anisotropy in the collision frequencies, using the parallel value here for simplicity. The effective gravity be denoted  $\mathbf{g} = -\nabla U$  and the pressures are  $P_j = n_j k_b T$ . The momentum equations for e, p and H are, respectively,

$$-en_e \left( \mathbf{E} + \frac{1}{c} \mathbf{v}_e \times \mathbf{B} \right) - \nabla P_e + n_e m_e [\mathbf{g} + \nu_{ep} (\mathbf{v}_p - \mathbf{v}_e) + \nu_{eH} (\mathbf{v}_H - \mathbf{v}_e)] = 0 \quad (\text{B1})$$

$$en_p \left( \mathbf{E} + \frac{1}{c} \mathbf{v}_p \times \mathbf{B} \right) - \nabla P_p + n_p m_p [\mathbf{g} + \nu_{pe} (\mathbf{v}_e - \mathbf{v}_p) + \nu_{pH} (\mathbf{v}_H - \mathbf{v}_p)] = 0 \quad (\text{B2})$$

$$-\nabla P_H + n_H m_p [\mathbf{g} + \nu_{He} (\mathbf{v}_e - \mathbf{v}_H) + \nu_{Hp} (\mathbf{v}_p - \mathbf{v}_H)] = 0. \quad (\text{B3})$$

In order, the terms in eq.B1 are the Lorentz force, the pressure gradient, gravitational force, and collision drag force between e-p and e-H. We further impose charge neutrality

$$n_e = n_p, \quad (\text{B4})$$

and define the center of mass velocity (used throughout the paper)

$$\mathbf{v} = \frac{n_e m_e \mathbf{v}_e + n_p m_p \mathbf{v}_p + n_H m_p \mathbf{v}_H}{m_e n_e + m_p n_p + m_p n_H} \simeq \frac{n_p \mathbf{v}_p + n_H \mathbf{v}_H}{n_p + n_H}, \quad (\text{B5})$$

where the second equality is valid in the  $m_e/m_p \ll 1$  limit.

The momentum transfer and cyclotron frequencies are given in Table 2. They are shown as a function of depth in Figure 17 using values of  $n_p$ ,  $n_H$ ,  $T$  and  $B = B_{J,\text{eq}}(R/r)^3$  for the hydrostatic model of the equatorial dead zone shown in Figure 10. For these parameters, the gyration frequencies are larger than the e and p collision frequencies over the entire  $H^+$  and H layers, implying motion of both e and p perpendicular to magnetic field lines is greatly restricted by



the magnetic field. Collisions with e are dominated by p well into the H layer, while H dominates collisions with p deeper than the H-H<sup>+</sup> transition. H atom collisions with p dominate over those from e.

For a hydrogen atom traveling at a typical speed  $c_H \simeq 10 \text{ km s}^{-1} (T/10^4 \text{ K})^{1/2}$ , the mean free path against collisions with p is  $\simeq c_H/\nu_{Hp} \simeq 10 \text{ km} (10^8 \text{ cm}^{-3}/n_p)$ . The proton density is sufficiently large that the mean free path is smaller than the scale height,  $\simeq r^2/\lambda R$ , over the entire range shown in Figure 10. We conclude that, due to proximity to the star, the high temperature and large scale height cause the density to be large enough that a fluid treatment is appropriate. The hot Jupiter magnetospheres discussed here are collisional, and the exobase is sufficiently distant from the planet to be of little practical importance. A corollary is that H atoms do not fly ballistically through the magnetosphere, and hence acceleration by stellar tidal gravity or radiation pressure does not cause acceleration of H atoms away from the planet (Lyman  $\alpha$  radiation pressure is only effective in a thin outer skin where Lyman  $\alpha$  optical depth is less than unity (Murray-Clay et al. 2009)). Rather, acceleration induces a drift velocity, which we now estimate.

Ignoring the  $\nu_{He}$  term in eq.B3, the ion-neutral drift velocity is

$$\mathbf{v}_H - \mathbf{v}_p \simeq \frac{1}{\nu_{Hp}} \left( \mathbf{g} - \frac{1}{n_H m_p} \nabla P_H \right). \quad (\text{B6})$$

For a simple estimate of the drift speed, we ignore the pressure gradient term, and use fiducial values  $g \simeq 10^3 \text{ cm s}^{-2}$  and  $\nu_{Hp} \simeq 1 \text{ s}^{-1}$ , giving  $v_H - v_p \sim 10 \text{ m s}^{-1}$ , and a drift time over a distance  $R_J$  of months. However, ignoring the pressure gradient is a poor approximation. In the H layer, hydrogen atoms provide the pressure support and so hydrostatic balance implies the quantity in parenthesis in eq.B6 is small. In the H<sup>+</sup> layer, *in photoionization equilibrium*, the same cancellation occurs, but for a different reason. There, both protons and electrons provide the pressure support, and so the proton scale height is  $\simeq 2k_b T/m_p g$ . But in photoionization equilibrium, eq.41 implies  $n_H \propto n_p^2$ , giving hydrogen scale height  $\simeq k_b T/m_p g$ , so that the terms in parenthesis in eq.B6 very nearly cancel. The deviations from photoionization equilibrium implies the drift velocity is proportional to a factor  $n_p/n_{\text{eq}}$  in the H<sup>+</sup> layer and  $n_{\text{eq}}/n_H$  in the H layer, and the drift velocity is much smaller than the naive estimate  $\simeq g/\nu_{Hp}$ , except near the H-H<sup>+</sup> transition. Hence the drift time over a distance  $\simeq R$  is much longer than the photoionization time of  $\simeq \text{hrs}$ , hence photoionization equilibrium is a good approximation, as little diffusion can occur in between photoionization events.

Next we discuss deviations from perfect flux freezing. To derive Ohm's law, we follow Braginskii (1965) and solve eq.B3 for  $v_H$ , plug the result into eq.B1, and change references frames from  $\mathbf{v}_e$  to  $\mathbf{v}$  in the Lorentz force, with the result

$$\mathbf{E} + \frac{1}{c} \mathbf{v} \times \mathbf{B} = \left( \frac{\mathbf{J} \times \mathbf{B}}{n_e e c} \right) \left[ \frac{\rho_p}{\rho} - \frac{\rho_H \nu_{He}}{\rho \nu_H} \right] + \frac{\rho_H}{\rho} \frac{1}{\nu_{Hc}} \left( \mathbf{g} - \frac{1}{\rho_H} \nabla P_H \right) \times \mathbf{B} + \frac{\mathbf{J}}{\sigma} + \frac{m_e}{e} \mathbf{g} \left( 1 + \frac{\nu_{eH}}{\nu_H} \right) - \frac{\nabla P_e}{e n_e} - \frac{\nu_{eH}}{\nu_H} \frac{\nabla P_H}{e n_e} \quad (\text{B7})$$

Here  $\nu_H = \nu_{He} + \nu_{Hp}$ ,  $\sigma^{-1} = (m_e/n_e e^2)(\nu_{ep} + \nu_{eH}\nu_{Hp}/\nu_H)$  is the conductivity,  $\rho_p = m_p n_p$ ,  $\rho_H = m_p n_H$ , and  $\rho \simeq \rho_p + \rho_H$ . The second term on the left hand side is due to induction. The terms on the right hand side are the Hall term, drift due to net force on the neutrals, the Ohmic term, the (small) term due to gravity on the electrons, the electron pressure gradient term, which gives rise to the charge separation field, and its correction due to collisions with neutrals. The second term on the right hand side may be put in the form of ‘‘ambipolar diffusion’’, in astrophysical parlance, by using the total momentum equation

$$\rho_H \mathbf{g} - \nabla P_H \simeq -\rho_p \mathbf{g} + \nabla (P_e + P_p) - \frac{1}{c} \mathbf{J} \times \mathbf{B}, \quad (\text{B8})$$

yielding a term

$$\frac{\mathbf{B} \times (\mathbf{J} \times \mathbf{B})}{\rho c^2 \nu_H} \quad (\text{B9})$$

on the right hand side.

Applying eq.B7 to compute magnetic field evolution requires knowledge currents and particle densities. As argued in Appendix A, the cross-field currents are zero in the dead zone if the Bernoulli constant is uniform at the base of the atmosphere. While true for the simple case considered in this paper (isothermal, hydrostatic equilibrium), non-isothermal conditions and/or fluid motion at the base may induce perpendicular currents.

We now discuss the relative size of terms in Ohm's law. In the H<sup>+</sup> layer, the Ohmic diffusivity is  $\eta = c^2/4\pi\sigma \simeq (c^2/4\pi)(m_e \nu_{ep}/n_e e^2) \simeq 10^7 \text{ cm}^2 \text{ s}^{-1} (T/10^4 \text{ K})^{3/2}$ , independent of density. Assuming Ohmic decay is balanced through the induction term, and that the currents are of order  $J \sim (c/4\pi)(B/r)$ , the required (center of mass) fluid velocity is  $v \sim \eta/r \sim 10^{-3} \text{ cm s}^{-1}$ , many orders of magnitude smaller than any characteristic velocity in the problem. Deep in the H layer, Figure 17 shows that the collision rates, and hence diffusivity, may increase by an order of magnitude. For nonzero cross field currents, the ratio of the Hall to the Ohmic term is roughly  $\sim \Omega_e/\nu_e \sim 10^4$ , where  $\nu_e \equiv \nu_{ep} + \nu_{eH}\nu_{Hp}/\nu_H$ . When significant cross field currents exist, the Hall drift speed can be much larger than the Ohmic drift speed, but still much smaller than the gas sound speed. Lastly, if the neutral drift speed has a cross field

component, the second term on the right hand side may generate a fluid velocity  $v \sim (\rho_H/\rho)(v_H - v_p)$ . This drift speed is much larger than the Ohmic drift speed, although it is still much smaller than the sound speed.

We conclude that, for the ionization models discussed in this paper, the ion-neutral drift velocity and deviations from flux freezing in the H and H<sup>+</sup> layers are small, and single-fluid MHD is a good approximation.

## REFERENCES

- Arras, P., & Bildsten, L. 2006, *ApJ*, 650, 394  
 Arras, P., & Socrates, A. 2009, arXiv:0901.0735  
 Ballester, G. E., Sing, D. K., & Herbert, F. 2007, *Nature*, 445, 511  
 Ben-Jaffel, L. 2007, *ApJ*, 671, L61  
 Ben-Jaffel, L. 2008, *ApJ*, 688, 1352  
 Ben-Jaffel, L., & Sona Hosseini, S. 2010, *ApJ*, 709, 1284  
 Braginskii, S. I. 1965, *Reviews of Plasma Physics*, 1, 205  
 Charbonneau, D., Brown, T. M., Noyes, R. W., & Gilliland, R. L. 2002, *ApJ*, 568, 377  
 Christensen, U. R., Holzwarth, V., & Reiners, A. 2009, *Nature*, 457, 167  
 Dalgarno, A., & McCray, R. A. 1972, *ARA&A*, 10, 375  
 Ehrenreich, D., Lecavelier Des Etangs, A., Hébrard, G., Désert, J.-M., Vidal-Madjar, A., McConnell, J. C., Parkinson, C. D., Ballester, G. E., & Ferlet, R. 2008, *A&A*, 483, 933  
 Feldman, U., Behring, W. E., Curdt, W., Schuehle, U., Wilhelm, K., Lemaire, P., & Moran, T. M. 1997, *ApJS*, 113, 195  
 Fortney, J. J., & Nettelmann, N. 2009, *Space Science Reviews*, 115  
 Fossati, L., et al. 2010, *ApJ*, 714, L222  
 García Muñoz, A. 2007, *Planet. Space Sci.*, 55, 1426  
 Gold, T. 1959, *J. Geophys. Res.*, 64, 1219  
 Gu, P.-G., Lin, D. N. C., & Bodenheimer, P. H. 2003, *ApJ*, 588, 509  
 Hapke, B. 1993, *Topics in Remote Sensing*, Cambridge, UK: Cambridge University Press, —c1993,  
 Heinemann, M., & Olbert, S. 1978, *J. Geophys. Res.*, 83, 2457  
 Kivelson, M. G., & Russell, C. T. 1995, *Introduction to Space Physics*, Edited by Margaret G. Kivelson and Christopher T. Russell, pp. 586. ISBN 0521451043. Cambridge, UK: Cambridge University Press, April 1995.,  
 Kopal, Z. 1978, *Astrophysics and Space Science Library*, 68,  
 Koskinen, T. T., Yelle, R. V., Lavvas, P., & Lewis, N. K. 2010, arXiv:1004.1396  
 Lai, D., Helling, C., & van den Heuvel, E. P. J. 2010, arXiv:1005.4497  
 Lamers, H. J. G. L. M., & Cassinelli, J. P. 1999, *Introduction to Stellar Winds*, by Henny J. G. L. M. Lamers and Joseph P. Cassinelli, pp. 452. ISBN 0521593980. Cambridge, UK: Cambridge University Press, June 1999.  
 Lecavelier Des Etangs, A., et al. 2010, *A&A*, 514, A72  
 Li, S.-L., Miller, N., Lin, D. N. C., & Fortney, J. J. 2010, *Nature*, 463, 1054  
 Linsky, J. L., Yang, H., France, K., Froning, C. S., Green, J. C., Stocke, J. T., & Osterman, S. N. 2010, arXiv:1005.1633  
 Lovelace, R. V. E., Mehanian, C., Mobarry, C. M., & Sulkanen, M. E. 1986, *ApJS*, 62, 1  
 Lubow, S. H., & Shu, F. H. 1975, *ApJ*, 198, 383  
 Mercier, C., & Heyvaerts, J. 1977, *A&A*, 61, 685  
 Mestel, L. 1968, *MNRAS*, 138, 359  
 Mestel, L., & Spruit, H. C. 1987, *MNRAS*, 226, 57  
 Mihalas, D. 1978, *San Francisco*, W. H. Freeman and Co., 1978. 650 p.,  
 Murray-Clay, R. A., Chiang, E. I., & Murray, N. 2009, *ApJ*, 693, 23  
 Murray, C. D., & Dermott, S. F. 2000, *Solar System Dynamics*, by C.D. Murray and S.F. Dermott, Cambridge, UK: Cambridge University Press, 2000.,  
 Noyes, R. W., & Kalkofen, W. 1970, *Sol. Phys.*, 15, 120  
 Osterbrock, D. E., & Ferland, G. J. 2006, *Astrophysics of gaseous nebulae and active galactic nuclei*, 2nd. ed. by D.E. Osterbrock and G.J. Ferland. Sausalito, CA: University Science Books, 2006  
 Okamoto, I. 1974, *MNRAS*, 166, 683  
 Parks, G. K. 2004, *Physics of space plasmas : an introduction / George K Parks*. Boulder, Colo. : Westview Press, Advanced Book Program, c2004.,  
 Pneuman, G. W., & Kopp, R. A. 1971, *Sol. Phys.*, 18, 258  
 Preusse, S., Kopp, A., Büchner, J., & Motschmann, U. 2007, *Planet. Space Sci.*, 55, 589  
 Sánchez-Lavega, A. 2004, *ApJ*, 609, L87  
 Schunk, R. W. & Nagy, A. F. 2004, *Ionospheres (Ionosphere)*  
 Spruit, H. C. 1996, arXiv:astro-ph/9602022  
 Stone, J. M., & Proga, D. 2009, *ApJ*, 694, 205  
 Tian, F., Toon, O. B., Pavlov, A. A., & De Sterck, H. 2005, *ApJ*, 621, 1049  
 Vidal-Madjar, A., Désert, J.-M., Lecavelier des Etangs, A., Hébrard, G., Ballester, G. E., Ehrenreich, D., Ferlet, R., McConnell, J. C., Mayor, M., & Parkinson, C. D. 2004, *ApJ*, 604, L69  
 Vidal-Madjar, A., Lecavelier des Etangs, A., Désert, J.-M., Ballester, G. E., Ferlet, R., Hébrard, G., & Mayor, M. 2003, *Nature*, 422, 143  
 —. 2008, *ApJ*, 676, L57  
 Winn, J. N., Suto, Y., Turner, E. L., Narita, N., Frye, B. L., Aoki, W., Sato, B., & Yamada, T. 2004, *PASP*, 56, 655  
 Wood, B. E., Redfield, S., Linsky, J. L., Müller, H.-R., & Zank, G. P. 2005, *ApJS*, 159, 118  
 Woods, T. N., Rottman, G. J., Bailey, S. M., Solomon, S. C., & Worden, J. R. 1998, *Sol. Phys.*, 177, 133  
 Yan, M., Sadeghpour, H. R., & Dalgarno, A. 1998, *ApJ*, 496, 1044  
 Yelle, R. V. 2004, *Icarus*, 170, 167  
 Yelle, R. V. 2006, *Icarus*, 183, 508